



Atmospheric Impact on Long Pulse Laser Detection and Ranging  
(LADAR) Systems

THESIS

Isaac B. Putnam, First Lieutenant, USAF  
AFIT-ENG-13-M-39

DEPARTMENT OF THE AIR FORCE  
AIR UNIVERSITY

***AIR FORCE INSTITUTE OF TECHNOLOGY***

---

Wright-Patterson Air Force Base, Ohio

DISTRIBUTION STATEMENT A.  
APPROVED FOR PUBLIC RELEASE; DISTRIBUTION UNLIMITED

The views expressed in this thesis are those of the author and do not reflect the official policy or position of the United States Air Force, Department of Defense, or the United States Government.

ATMOSPHERIC IMPACT ON LONG PULSE LASER DETECTION AND RANGING  
(LADAR) SYSTEMS

THESIS

Presented to the Faculty

Department of Electrical and Computer Engineering

Graduate School of Engineering and Management

Air Force Institute of Technology

Air University

Air Education and Training Command

In Partial Fulfillment of the Requirements for the  
Degree of Master of Science in Electrical Engineering

Isaac B. Putnam, BS

First Lieutenant, USAF

March 2013

APPROVED FOR PUBLIC RELEASE; DISTRIBUTION UNLIMITED

ATMOSPHERIC IMPACT ON LONG PULSE LASER DETECTION AND RANGING  
(LADAR) SYSTEMS

Isaac B. Putnam, BS  
First Lieutenant, USAF

Approved:



Dr. Stephen C. Cain, PhD (Chairman)

7 Feb 2013

Date



Milo W. Hyde, Maj, USAF (Member)

7 Feb 2013

Date



Dr. Victor Gamiz, PhD (Member)

7 Feb 2013

Date

## **Abstract**

For conventional imaging systems, geosynchronous earth orbit (GEO) space objects cannot be resolved due to their 40 Mm distance. There exists a strong need to obtain high resolution images of GEO objects and to accomplish this task, investigation into the suitability of inverse synthetic aperture laser radar (ISAL) is currently underway. A critical component in determining this suitability is to accurately model the atmospheric impacts on laser detection and ranging (LADAR) pulses. The expected result is that atmospheric impacts are a strong function of the illumination beam length.

Conventional knowledge says that while the atmosphere churns, wind is the predominant cause of temporal evolution which simplifies all modeling and simulation into the frozen flow hypothesis. The concern is that the frozen flow hypothesis based phase screen generation techniques fail to accurately predict the temporal development of optical phase. Additionally, wavefront phase aberrations introduced by the atmosphere are dominated by tilt, which is often underrepresented in the frozen flow approximation and causes the most degradation of direct-detection LADAR system performance.

This thesis proposes a new approach and provides a detailed derivation of a new temporally evolving Zernike polynomial based atmospheric phase screen generation model. This new model is verified through laboratory experiment, and then utilized to analyze atmospheric effects on long pulse LADAR beams and their impact on mixing efficiencies. It is shown that this new turbulent flow model more accurately predicts mixing efficiency than that of the basic frozen flow approximation.

## **Acknowledgments**

I would like to earnestly thank Dr. Stephen Cain for his guidance which has been crucial to the development of this research. Dr. Cain always demonstrated unparalleled dedication and enthusiasm when assisting me. I hope that I have gleaned some of his professionalism and research methodologies. I would also like to thank my committee members, Maj Milo Hyde and Dr. Victor Gamiz, for taking me on as a student; both have a wealth of knowledge and have been truly remarkable resources. I consider myself entirely fortunate to have these three subject matter experts on my committee.

Isaac B. Putnam

# Table of Contents

	Page
Abstract.....	iv
Acknowledgments.....	v
Table of Contents.....	vi
List of Figures.....	viii
List of Tables.....	x
List of Equations.....	xi
I. Introduction.....	1
1.1 Problem Statement and Hypothesis.....	1
1.2 Research Focus.....	2
1.3 Thesis Overview.....	3
II. Background Theory.....	4
2.1 Inverse Synthetic Aperture LADAR (ISAL).....	4
2.2 System Overview.....	5
2.3 Atmospheric Model.....	6
2.3.1 FFT-based Phase Screen Generation.....	7
2.3.2 Zernike-based Phase Screen Generation.....	8
2.4 Mixing Efficiency.....	11
2.5 Chapter Summary.....	12
III. Temporal Correlation.....	13
3.1 Expanding the Random Walk Algorithm.....	13
3.2 Temporal Evolution of Zernike-based Phase Screens.....	18
3.3 Chapter Summary.....	19
IV. Model Evaluation.....	20
4.1 Laboratory Experiment Configuration.....	20
4.1.1 Point Source.....	21
4.1.2 Optics.....	21
4.1.3 Turbulent Medium.....	22
4.2 Extracting $r_0$ .....	23
4.2.1 Maximum Correlation.....	23
4.2.2 Gerchberg-Saxton Phase Retrieval.....	24

4.2.3 Results of Extracting $r_0$ .....	25
4.3 Comparing Recorded, Simulated, and Theoretical Tilt Correlation in Time.....	26
4.4 Chapter Summary.....	28
V. Simulation Analysis and Results.....	29
5.1 Simulation Environment .....	29
5.1.1 Atmosphere .....	30
5.1.2 Sub Pixel Shifting.....	35
5.1.3 Coherent Illumination Beam .....	36
5.1.4 System Integration.....	36
5.2 Modulation Efficiency as the Pulse Length Varies.....	38
5.2.1 Total Atmospheric Change.....	39
5.2.2 Mixing Efficiency Results.....	43
5.3 Chapter Summary.....	44
VI. Conclusions and Recommendations.....	45
6.1 Summary .....	45
6.2 Conclusions of Research.....	46
6.3 Significance of Research.....	46
6.4 Recommendations for Future Research .....	47
6.5 Chapter Summary.....	48
Appendix A – Zernike-based Mixing efficiency .....	49
Appendix B – FFT-based Mixing efficiency .....	51
Bibliography .....	53



## List of Figures

	Page
Figure 1: FFT-based phase screen generation. ....	7
Figure 2: FFT-based phase screen. ....	8
Figure 3: Zernike-based phase screen. ....	10
Figure 4: Interferometer functionality. ....	11
Figure 5: Experimental configuration. ....	20
Figure 6: Camera and optics. ....	22
Figure 7: Gerchberg-Saxton algorithm. ....	24
Figure 8: Phase extracted from raw data. ....	25
Figure 9: Maximum correlation $r_0$ fitting. ....	25
Figure 10: Mean squared error $r_0$ fitting. ....	26
Figure 11: Theoretical OTF compared to Fourier (left) & Zernike (right). ....	28
Figure 12: Atmosphere's structure. ....	30
Figure 13: Zernike phase screens representing atmospheric layers. ....	32
Figure 14: FFT phase screens representing atmospheric layers. ....	33
Figure 15: Total Zernike-based phase, representing 8 atmospheric layers. ....	34
Figure 16: Total FFT-based phase, representing 8 atmospheric layers. ....	34
Figure 17: Atmospheric effects over 10 $\mu$ sec pulse. ....	37
Figure 18: Atmospheric effects over 100 $\mu$ sec pulse. ....	38
Figure 19: Total atmospheric change in Zernike-based (top) and FFT-based (bottom). ..	40
Figure 20: Zernike-based $\theta_{atm\Delta}$ over 10 $\mu$ sec pulse (top) and 100 $\mu$ sec pulse (bottom). ..	41
Figure 21: FFT- based $\theta_{atm\Delta}$ over 10 $\mu$ sec pulse (top) and 100 $\mu$ sec pulse (bottom). ....	42

Figure 22: Average mixing efficiency with logarithmic trend lines..... 43

## List of Tables

	Page
Table 1: Tilt correlation in time .....	27
Table 2: Zernike-based mixing efficiency .....	50
Table 3: FFT-based mixing efficiency.....	52

## List of Equations

	Page
Equation 1: Modified von-Kármán spectrum .....	7
Equation 2: Idealized von-Kármán spectrum .....	8
Equation 3: Definition of Zernike polynomials .....	9
Equation 4: Radial function definition.....	9
Equation 5: Zernike phase screen .....	9
Equation 6: Definition of $a_j$ vector .....	9
Equation 7: Cholesky factorization.....	9
Equation 8: Covariance matrix .....	10
Equation 9: Definition of $K_{zz}$ .....	10
Equation 10: Conditional delta function .....	10
Equation 11: Average interferometer intensity.....	12
Equation 12: Bayes' conditional density .....	14
Equation 13: Standard bivariate Gaussian .....	14
Equation 14: Marginal density function .....	14
Equation 15: Expanded joint density function.....	15
Equation 16: $\tilde{n}$ vector conditional mean .....	15
Equation 17: $\tilde{n}$ vector conditional variance .....	15
Equation 18: Base definition of $R_n(\delta_t)$ .....	15
Equation 19: Tilt correlation at time, $t=0$ .....	15
Equation 20: Tilt correlation at time, $t=0+\Delta t$ .....	15
Equation 21: $R_n(\delta_t)$ expanded.....	16

Equation 22: $R_n(\delta_t)$ expanded and rearranged.....	16
Equation 23: $R_n(\delta_t)$ expanded by change of variable .....	16
Equation 24: First Fourier correlation.....	17
Equation 25: Second Fourier correlation .....	17
Equation 26: $P_{k,l}$ correlation of aperture with Zernike polynomial .....	17
Equation 27: $R_n(\delta_t)$ in terms of $R_\theta$ correlation .....	17
Equation 28: Phase structure-correlation relationship .....	17
Equation 29: $D_n(\delta_t)$ in terms of phase correlations .....	17
Equation 30: $D_n(\delta_t)$ in terms of structure difference .....	18
Equation 31: Phase structure function .....	18
Equation 32: Maximum spatial frequency for circular aperture .....	21
Equation 33: Lensmaker's equation.....	21
Equation 34: Convective air velocity.....	23
Equation 35: Cross correlation of real-valued signals .....	23
Equation 36: Theoretical tilt in time .....	26
Equation 37: Theoretical tilt correlation in time.....	27
Equation 38: Far field propagation criteria .....	31
Equation 39: Fourier shift theorem .....	35
Equation 40: Sub pixel shift.....	35
Equation 41: Euler's formula.....	35
Equation 42: Total control intensity .....	38
Equation 43: Total test intensity .....	38
Equation 44: Test beam .....	38

Equation 45: Control beam .....	38
Equation 46: Mixing efficiency .....	39

# Atmospheric Impact on Long Pulse Laser Detection and Ranging (LADAR) Systems

## I. Introduction

Imaging otherwise non-resolvable Geosynchronous Earth Orbiting (GEO) objects with Inverse Synthetic Aperture Laser detection and ranging (LADAR), or ISAL is currently the focus of a recent Air Force Research Laboratory (AFRL) effort. ISAL acquires images of a coherently illuminated target as it traverses the sky. This synthesizes a much larger aperture than that of the observatory and through post processing, permits the construction of high resolution images. Considering the 3.67 m primary mirror of the Advanced Electro Optical System (AEOS), and a typical operating wavelength  $\lambda$  of 0.5  $\mu\text{m}$ , the minimal resolvable angle  $A_\theta$  is equal to  $A_\theta = 1.22\lambda/3.67$ , or roughly 0.1667  $\mu\text{rad}$ . Transposing that to the smallest resolvable object at a typical GEO distance of 40 Mm equates to approximately 6.5 meters. The largest of GEO satellites therefore occupy no more than a few pixels of an image. ISAL is intended to overcome the physical limitations of meter class telescopes such as the AEOS.

### 1.1 Problem Statement and Hypothesis

This thesis evaluates the atmospheric impacts on long pulse LADAR systems, a manageable portion of the much larger ISAL problem. More specifically, this thesis analyzes mixing efficiencies as a function of the pulse length. The analysis provided herein aids in the investigation of ISAL.

Conventional knowledge implies atmospheric impacts are a strong function of the illumination wavelength and beam duration. The often ignored additional dimension of temporal evolution, the boiling and churning of turbulence, is the primary focus of this thesis. Even during the relatively long beam pulses used in ISAL, the atmosphere simply does not have time to “shift” according to the frozen flow hypothesis approximation. Note that ISAL utilizes a chirped waveform, which is paraphrased as a pulse within this thesis. Consider for a moment a 100  $\mu$ sec long pulse where the combined and prevailing wind is 10 m/sec. If prognostic analysis is limited to frozen flow, then the atmosphere will shift a single millimeter during that pulse. For shorter pulse lengths, lower wind speeds, or a combination of the two, the superficial shift is even less significant. It is expected that the affects of the atmosphere upon the pulse are directly related to the illumination wavelength and the duration of the pulse.

## **1.2 Research Focus**

It is hypothesized that since the atmosphere cannot flow by any considerable amount on these time scales, perhaps it can boil, or churn. Therefore, the critical component of this thesis is the development of a new, accurate atmospheric phase screen generation technique that not only shifts as the frozen flow model does, but also evolves. This new model permits realistic atmospheric evolution during the relatively short pulses of spotlight-mode ISAL illumination, and ultimately the detection and imaging of GEO space objects.

The predominate focus of this research is the development and validation of the new temporal phase screen generation model. As previously mentioned, it is expected



that atmospheric impacts are a function of the ISAL system's pulse lengths. This new, unique and useful tool should not only verify such conventional understanding, but can be used in numerous applications, particularly within LADAR based applications. This model is validated through laboratory experiment in which recorded data will be collected, then compared to theoretical as well as the new and commonly used models. The modeling and simulation, recorded lab data analysis, and subsequent validation are performed within the `Matlab`<sup>®</sup> environment.

### **1.3 Thesis Overview**

Following this brief introductory chapter, Ch. II provides an introduction to ISAL, simulating atmospheric turbulence with phase screens, and mixing efficiency. Two principal existing methods of phase screen simulation are discussed: Fourier-based and Zernike-based approaches. The development of temporal correlation of the new Zernike-based turbulent-flow phase screen generation is the topic of Ch. III. The laboratory configuration which provides measured data for the new model's comparison is discussed in Ch. IV as well as the results of this with comparative analysis. The methodologies of simulation used to achieve the objectives of Sec. 1.2 are discussed in Ch. V, as well as a presentation and discussion of the findings. Finally, Ch. VI summarizes the research efforts of this thesis, discusses the challenges, critical results, and provides guidance for future related research efforts.

## II. Background Theory

This chapter introduces the basic concepts and components of the ISAL system that are modeled into simulation for subsequent analysis. Basic phase screen generation techniques are discussed in terms of simulating atmospheric turbulence, with particular emphasis on the Zernike polynomial-based approach. This is because Ch. III develops the new model based on the basic Zernike theory provided here. Additionally, an overview of the system is presented, highlighting the relevant concepts of interferometry and its application to mixing efficiency.

### 2.1 Inverse Synthetic Aperture LADAR (ISAL)

Conventional imaging systems require a 10m class or larger aperture to provide useful information of distant GEO objects [12]. Synthetic aperture systems rely on relative movement between the target and observation point to effectively synthesize a larger aperture. This permits cost savings by utilizing smaller optics. Where synthetic aperture radar (SAR) systems rely on a moving observer with a static target, ISAL conversely relies on a moving target with static observation.

ISAL has three key characteristics which differentiate it from these previously proposed solutions: tomographic imaging techniques, coherent illumination and heterodyne detection, and utilizing a chirped ISAL waveform [12]. These three characteristics in combination are expected to permit high resolution imaging. Utilizing coherent illumination allows for tomographic reconstruction from the Fourier data, and in combination with heterodyne detection, provides methods for boosting the signal to noise ratio (SNR).

## 2.2 System Overview

While utilizing ISAL eliminates the difficulty and cost of obtaining a 10m class telescope, it requires actively illuminating GEO objects and coherently detecting the return signal. The process of active illumination incurs atmospheric perturbations of both the outbound and return waveform. However the atmosphere effectively ends at 600km, 1.5% of the 40 Mm distance. As such, regardless of any irradiance fluctuations, beam spreading, or loss of spatial coherence of the outbound wavefront the remaining 39.4 Mm vacuum propagation ensures that even the largest GEO satellites are uniformly and coherently illuminated [1]. Therefore, as the goal is to determine the mixing efficiencies as the pulse length varies, the simulation may be modeled as a one-directional, illuminated-GEO-object-to-observation-point propagation. Pulse length dictates the duration in which light propagates through the atmosphere, directly limiting the time for the atmosphere to evolve. It is during this period that relative phase differences between the transmitted and reference beams affect mixing efficiencies.

It is readily understood that even the most impressive adaptive optics (AO) systems, such as those within the AEOS, cannot continuously and fully correct wavefront perturbations. If the AO system could fully compensate then there would be no losses in mixing efficiency. This uncorrectable time interval in which modulation efficiency losses occur is what concerns AFRL. Recall that if temporal evolution is limited to a frozen flow approximation, the AO system will require minimal to no compensation due to nearly non-existent shift.

The ISAL system is expected to be integrated into the 3.67m class AEOS at the Air Force Maui Optical and Supercomputing (AMOS) observatory, where some of the

best seeing in the world is common. A seeing parameter (Fried's constant), or  $r_0$ , of 14 cm is typical and is the value utilized in simulating the objectives of Sec. 1.2. The GEO object will effectively be modeled as a point source illuminated by varying pulse lengths with a visible wavelength  $\lambda = 550$  nm. The GEO object illumination propagates through a discrete number of independently evolving phase screens to the 3.67m aperture as described in Sec 5.1.1. Then after propagating to the detector plane, the measured test beam is combined with the control beam to measure mixing efficiency.

### 2.3 Atmospheric Model

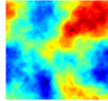
Turbulence is largely located within relatively few narrow concentrated layers at good astronomical sites such as AMOS [1]. Consider for a moment a critical component of optical imaging systems: lenses. While a lens can converge, diverge, focus and disperse light, the most important property of a lens is the phase transformation introduced to the propagating light [6]. A lens in which light enters and exits at approximately the same transaxial coordinates is referred to as a thin lens. Thin lenses primarily delay the incident wavefront proportional to the thickness of the lens at each coordinate. In this sense, thin lens approximations of atmospheric turbulence and phase screens are synonymous. This discrete modeling of the atmosphere is permitted by the profile of the structure constant of  $C_n^2(h)$ , the refraction index fluctuations, with discrete values of height  $h$  [1]. The layers of atmospheric turbulence are simulated with random phase screens whose power spectrum follows a Kolmogorov model.

Two common phase screen generation models are comparatively analyzed for the objectives outlined in Sec 1.2.: the fast-Fourier-transform (FFT)-based method and the

Zernike polynomial-based method. Other methods such as the Fourier series model will not be analyzed as they use the same frozen flow temporal evolution that the FFT method does [15]. The FFT-based method will provide comparison of frozen flow approximation to the new Zernike-based turbulent flow results. The basic Zernike-based theory presented here is expanded to provide temporal evolution in Ch. III.

### 2.3.1 FFT-based Phase Screen Generation

The FFT-based methods are quite common since very large phase screens may be generated quickly. FFT-based methods are similar in that they are generated from their respectively named power spectral densities (PSDs). Put simply, these screens are generated by taking the inverse FFT of the square root of the PSD multiplied by a random zero mean, unit variance matrix. See Fig. 1 for a basic visualization of this process.

$$\mathcal{F}^{-1} \left\{ \begin{array}{|c|} \hline \text{Zero } \mu, \\ \text{unit } \sigma, \\ \text{matrix} \\ \hline \end{array} \times \begin{array}{|c|} \hline \sqrt{PSD} \\ \hline \end{array} \right\} = \text{Phase Screen}$$


**Figure 1: FFT-based phase screen generation.**

One well known disadvantage of this approach is that lower-order aberrations such as tilt are often under-represented [14]. These lower-order aberrations make up a majority of the atmospheric energy spectrum and as such, must be included to produce realistic models. One of the more widely used FFT-based methods is that of the modified von-Kármán spectrum,

$$\Phi(\kappa) = 0.023(r_0)^{-5/3} e^{-\left(\frac{\kappa}{\kappa_m}\right)^2} (\kappa^2 + \kappa_0^2)^{-11/6}. \quad (1)$$

The modified von-Kármán, allows an application of the inner ( $l_0$ ) and outer ( $L_0$ ) scales of turbulent eddies, leading to  $\kappa_m = 5.92/l_0$ , and  $\kappa_0 = 2\pi/L_0$ , in which  $\kappa$  is the spatial

frequency and is scaled by a factor of Fried's constant,  $r_0$ . This investigation assumes ideal limits where  $L_0$  approaches infinity and  $l_0$  approaches zero, as this best reflects the inner and outer scales of the subsequently discussed Zernike-based method. With these inner and outer scales, Eq. (1) reduces to Eq. (2).

$$\Phi(\kappa) = 0.023(r_0)^{-5/3}(\kappa^2)^{-11/6} \quad (2)$$

A sample screen generated by this method is shown in Fig. 2. Discussion of generating FFT-based screens is limited to this point as they are well known [9], [14], [15], and only utilized for comparative analysis. Further discussion and methodology for generating FFT-based frozen flow approximation phase screens is readily available.

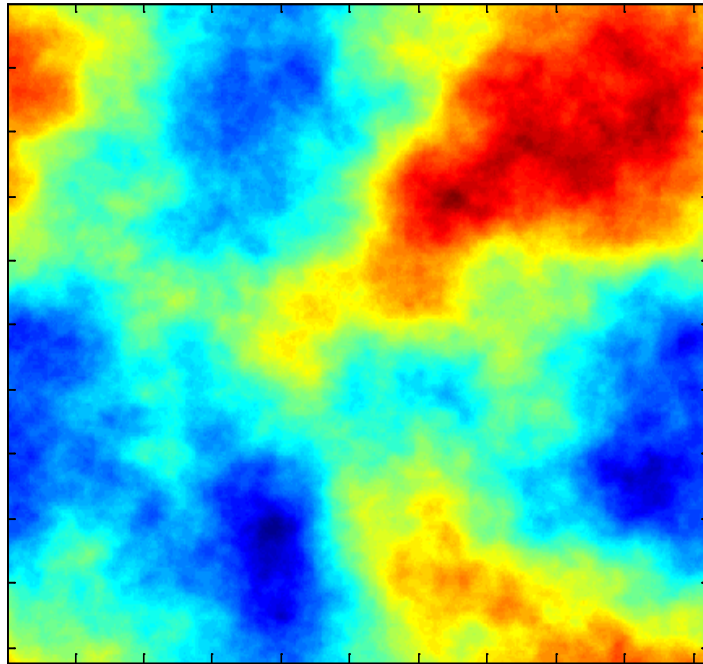


**Figure 2: FFT-based phase screen.**

### ***2.3.2 Zernike-based Phase Screen Generation***

Drawing a stark contrast to Fourier methods, the Zernike polynomial approach does not begin with a random phase array. Instead coefficients are combined into two-

dimensional random functions. In his 1976 paper, Noll [10] defined a new modified set of Zernike polynomials,  $Z_j(r, \theta)$ . He defined these polynomials to be

$$\left. \begin{aligned} Z_{\text{even } j}(r, \theta) &= \sqrt{n+1} S_n^m \sqrt{2} \cos(m\theta) \\ Z_{\text{odd } j}(r, \theta) &= \sqrt{n+1} S_n^m \sqrt{2} \sin(m\theta) \end{aligned} \right\}, \quad m \neq 0 \quad (3)$$

$$Z_j(r, \theta) = \sqrt{n+1} S_n^0(r), \quad m = 0$$

where the functions  $S_n^m(r)$  are referred to as radial functions and are defined as

$$S_n^m(r) = \sum_{s=0}^{\frac{n-m}{2}} \frac{(-1)^s (n-s)!}{s! [(n+m)/2 - s]! [(n-m)/2 - s]!} r^{n-2s}. \quad (4)$$

This function is based on a polar coordinate system where  $S$  is the radius,  $r$  is the position along the radius, and  $\theta$  is the angle with respect to the  $x$ -axis. Noll's numbering sequence of the index  $j$  corresponding to each polynomial  $Z_j$  proceeds by row, then value of radial degree  $n$ , and increases with azimuthal frequency  $m$ . Combining these equations, it is then possible to generate independent, random phase screens  $\theta_{atm}$  from the relationship

$$\theta_{atm}(Sr, \theta) = \sum_{j=1}^J a_j Z_j(r, \theta). \quad (5)$$

To generate the phase screen with accurate correlation it is necessary to calculate the coefficient amplitude vector  $a_j$  by multiplying  $\underline{\Phi}$  with a zero-mean, unit-variance random vector  $\vec{n}$ . The  $\vec{n}$  vector has a length equal to  $J$ . The  $a_j$  vector is defined as

$$a_j = \underline{\Phi} \vec{n}, \quad (6)$$

where  $\underline{\Phi}$  is the Cholesky decomposition of the covariance matrix,

$$\underline{\Phi} = \sqrt{\underline{C}} \quad \text{and} \quad \underline{\Phi}^T \underline{\Phi} = \underline{C}. \quad (7)$$

The covariance matrix  $C$  is generated from the covariance of any two Zernike polynomial coefficients  $a_j$  and  $a_{j'}$  [13] as provided in Eq. (8):

$$C_{j,j'} = E[a_j, a_{j'}] = \frac{K_{zz'} \delta_z \Gamma[(n+n'-5/3)/2] (D/r_0)^{5/3}}{\Gamma[(n-n'-17/3)/2] \Gamma[(n-n'-17/3)/2] \Gamma[(n+n'-23/3)/2]} \quad (8)$$

in which

$$K_{zz'} = \frac{\Gamma\left(\frac{14}{3}\right) \left[\left(\frac{24}{5}\right) \Gamma\left(\frac{6}{5}\right)\right]^{\frac{5}{6}} \left[\Gamma\left(\frac{11}{6}\right)\right]^2}{2\pi^2} \times (-1)^{\frac{(n+n'-2m)}{2}} \sqrt{(n+1)(n'+1)} \quad (9)$$

and

$$\delta_z = (m = m') \bigwedge \left[ \overline{\text{parity}(j, j')} \vee (m = 0) \right]. \quad (10)$$

An example of a phase screen generated by this method using 1,024 Zernike polynomials is provided in Fig. 3.

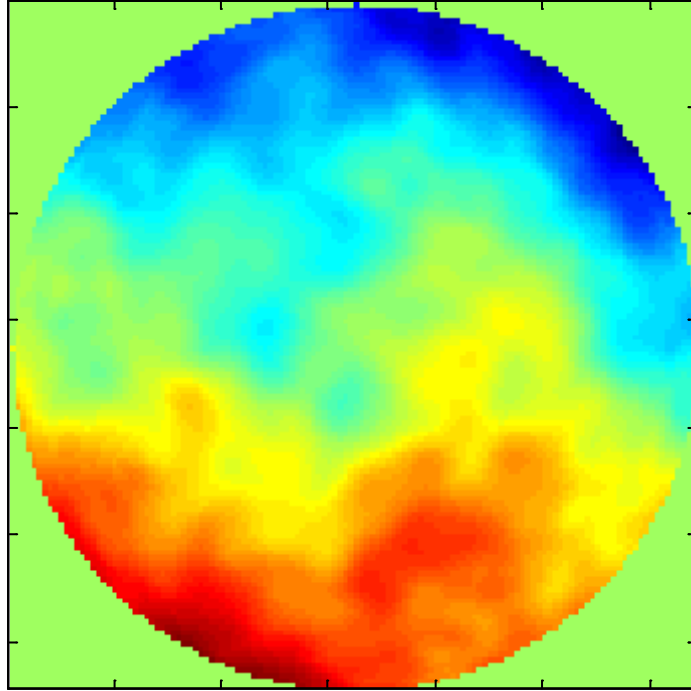


**Figure 3: Zernike-based phase screen.**



## 2.4 Mixing Efficiency

Mixing efficiency, referenced interchangeably with modulation efficiency throughout this text, is the percent efficiency of combining a test signal with a control signal. It should be accentuated that analysis of mixing efficiency has not previously been accomplished in terms of ISAL application. The illumination signal is split and then later combined by interferometers, or beam splitters, as Fig. 4 depicts.

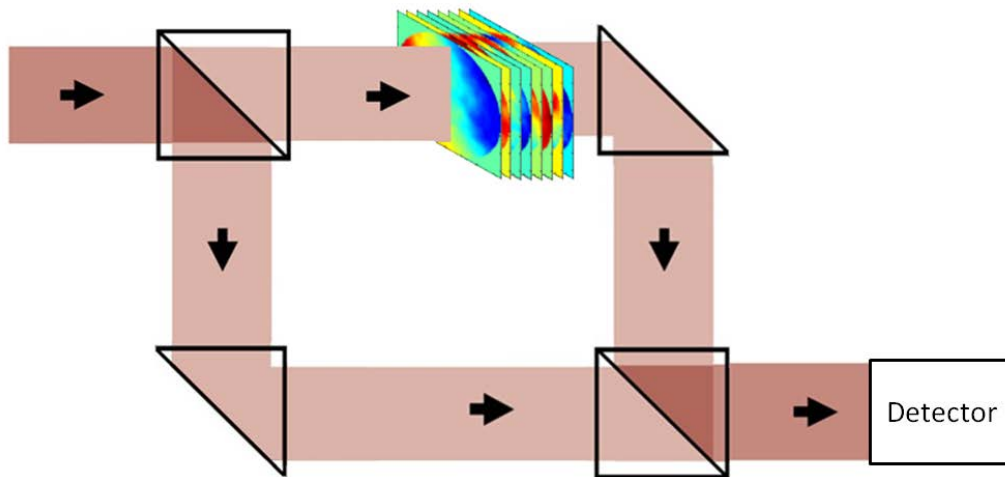


**Figure 4: Interferometer functionality.**

The intended application in regards to ISAL involves boosting the target return signal SNR by adding it to an undistorted and delayed control signal. In other words, mixing efficiency is the percent efficiency in which a split beam propagated through different paths, may be recombined. Conventional knowledge assumes that obtainable modulation efficiencies are approximately 10%. Sec 5.2 provides the mathematical methodology for accomplishing this analysis. For the purposes of this introduction, mixing efficiency is defined as the fraction of test beam intensity minus the bias, all of which is divided by the bias; where the bias is half of the control beam intensity. The control intensity is calculated by combining the intensity of two vacuous far-field propagated point sources,

subsequently synonymous with control beams. The test intensity is calculated by combining the intensity of a vacuum far-field propagated point source with the intensity of point source propagated through turbulence [8]. The intensity  $I_D$  incident on the detector  $D$  when taking account for the relative time delay,  $2h/c$ , where  $h$  is the pathlength and  $c$  is the speed of light, can be written as

$$I_D(h) = \left\langle \left| K_1 \mathbf{u}(t) + K_2 \mathbf{u} \left( t + \frac{2h}{c} \right) \right|^2 \right\rangle, \quad (11)$$

where  $K_1$  and  $K_2$  are real numbers determined by the losses in the two paths and  $\mathbf{u}(t)$  is the analytic signal representation of the light emitted by the source [7].

## 2.5 Chapter Summary

In summary, the ISAL system may be simplified into a one-directional, GEO-object-to-observatory-point-source propagation. Atmospheric turbulent layers will be represented by the FFT- and Zernike-based phase screens previously described, and will be temporally evolved by their individual means as detailed in Sec. 5.1.2 and Ch. 3 respectively. The pulse lengths dictate the duration of light traveling through the atmosphere, which in turn directly effects the time in which the atmosphere may evolve. It is during these brief pulses that attempting to combine the propagated beam with a control beam will effectively measure the theoretical mixing efficiency.

### **III. Temporal Correlation**

This chapter builds upon the understanding of Zernike-based phase screen generation discussed in Sec 2.3.2, providing the ability for statistically accurate temporal evolution of a phase screen not limited to the frozen flow approximation. Atmospheric layers are modeled into the simulation by two dimensional phase screens representing respective layers of turbulence. This alternating free-space diffraction and phase screen accumulation represents the effect of propagating through an extended volume of turbulence. The Zernike-based approach is utilized because traditional, FFT-based phase screens are limited to frozen flow evolution. Without determining the factor of correlation between individual pixels, the FFT methods can only shift, not evolve, with statistical accuracy. In the application of ISAL, the atmosphere cannot shift any significant distance. Yet atmospheric effects are still observed, thus, the need to investigate a new model that permits turbulent flow. This chapter develops the means to generate a phase screen that evolves as it shifts to overcome the shortfall of frozen flow limitations.

#### **3.1 Expanding the Random Walk Algorithm**

The benefit of the Zernike-based method is that once a single random screen is generated, the correlation between each pixel is inherent within the Zernike polynomials. Cain's [3] work with atmospheric tilt has already generated a statistically accurate algorithm to temporally evolve tilt, the second and third Zernike polynomials. By expanding this algorithm from these two polynomials to any  $N$  maximum number of Zernike polynomials and utilizing the methodology of the expanded algorithm, the

generation of a temporal correlation of the  $\vec{n}$  vector is computed. Updating the  $\vec{n}$  vector is much more computationally efficient than it is to update the  $a_j$  vector, as the  $\vec{n}$  vector is independent and identically distributed (IID). With a temporally correlated  $\vec{n}$  vector, the  $a_j$  vector can evolve accurately and in turn, contiguous phase screens may evolve. The expansion of the random walk algorithm begins by utilizing Bayes' theorem of the conditional density function Eq. (12),

$$f_{(n(t_{k+1})|n(t_k))}(x|y) = \frac{f_{n(t_{k+1}),n(t_k)}(x,y)}{f_{n(t_k)}(y)} \quad (12)$$

in which the joint density function  $f_{(n(t_{k+1}),n(t_k))}(x,y)$  is zero mean Gaussian,  $t_k$  and  $t_{k+1}$  are two different observation times, and  $n(t_k)$  is a single element of the  $\vec{n}$  vector at time  $t_k$ . By denoting  $E[n(t_k)^2] = E[n(t_k + 1)^2]$  as  $R_n(0)$  and  $E[n(t_k)n(t_k + 1)]$  as  $R_n(\delta_t)$ , where  $\delta_t = t_k + 1 - t_k$ , the joint density assumes the standard bivariate Gaussian form [2]:

$$f_{n(t_{k+1}),n(t_k)}(x,y) = \frac{1}{2\pi[R_n^2(0) - R_n^2(\delta_t)]^{\frac{1}{2}}} \times e^{\left(\frac{-R_n^2(0)}{2(R_n^2(0) - R_n^2(\delta_t))} \left[ \frac{y^2}{R_n(0)} - \frac{2R_n(\delta_t)xy}{R_n^2(0)} + \frac{x^2}{R_n(0)} \right] \right)} \quad (13)$$

The marginal density function  $f_{n(t_k)}(y)$  has the standard form of a Gaussian random variable as provided in Eq. (14).

$$f_{n(t_k)}(y) = \frac{e^{-y^2/2R_n(0)}}{\sqrt{2\pi R_n(0)}} \quad (14)$$

By substituting Eq. (13) and Eq. (14) into Eq. (12) the expanded conditional density function is redefined as

$$f_{n(t_{k+1})|n(t_k)}(x|y) = \frac{1}{\sqrt{2\pi(R_n^2(0) - R_n^2(\delta_t))/R_n(0)}} \times e^{\left(-\frac{R_n(0)}{2(R_n^2(0) - R_n^2(\delta_t))} \left(x - \frac{yR_n(\delta_t)}{R_n(0)}\right)^2\right)}. \quad (15)$$

From this expanded conditional density, the conditional mean, Eq. (16), and the conditional variance, Eq. (17), of  $n(t_k + 1)$  given  $n(t_k)$  necessary to update the  $\vec{n}$  vector are extracted:

$$\mu_{n(t_{k+1})|n(t_k)} = \frac{n(t_k)R_n(\delta_t)}{R_n(0)} \quad (16)$$

$$\sigma_{n(t_{k+1})|n(t_k)}^2 = \frac{(R_n^2(0) - R_n^2(\delta_t))}{R_n(0)}. \quad (17)$$

Of significance at this point is the mathematical representation of the correlation of the  $\vec{n}$  vector in time  $R_{\vec{n}}(\delta_t)$ , which once computed provides the ability to update the phase screens while maintaining both correlation and randomness. The conditional mean in Eq. (16) can be rewritten as an expectation:  $\mu_{n(t_{k+1})|n(t_k)} = E[\vec{n}(t_2)|\vec{n}(t_1)]$ . By substitution of the inverse definition of the  $\vec{n}$  vector from Eq. (6),  $\vec{n} = \underline{\underline{\Phi}}^{-1}a_j$ , the correlation between elements of the  $\vec{n}$  vectors can therefore be defined as

$$R_{\vec{n}_j}(\delta_t) = E \left[ \left( \sum_{k=1}^N \underline{\underline{\Phi}}_{j,k}^{-1} a_k(t_1) \right) \left( \sum_{l=1}^N \underline{\underline{\Phi}}_{j,l}^{-1} a_l(t_2) \right) \right]. \quad (18)$$

Solving for the accurate correlation requires substitution of the  $a$ 's defined by [3] which expands Eq. (18) by the definitions of  $a_{j,k}$  and  $a_{j,l}$  in Eq. (19) and Eq. (20), respectively:

$$a_{j,k}(t_1) = \frac{\int \int A(w, s) \varphi_{j,k}(w, s) \Theta_{atm}(w, s) dw ds}{\int \int A(w, s) \varphi_{j,k}^2(w, s) \partial w \partial s} \quad (19)$$

$$a_{j,l}(t_2) = \frac{\int \int A(w, s) \varphi_{j,l}(w, s) \Theta_{atm}(w + (v_x)\delta_t, s + (v_y)\delta_t) \partial w_2 \partial s_2}{\int \int A(w, s) \varphi_{j,k}^2(w, s) \partial w \partial s}. \quad (20)$$

The aperture is represented as  $A$  and the random atmospheric phase screen as  $\theta_{atm}$ , each with the same coordinate system  $(w,s)$ . Note that  $a_{j,k}$  is considered to be at  $t = 0$  and  $a_{j,l}$  is at time  $t = 0 + \delta_t$ , where  $\delta_t$  is the difference in time. Finally,  $v_x$  and  $v_y$  are wind velocities. With this substitution, observatory parameters, and atmospheric conditions are included in the definition of  $R_{\bar{n}_j}(\delta_t)$  provided in Eq. (21):

$$R_{\bar{n}_j}(\delta_t) = E \left[ \left( \sum_{k=1}^N \underline{\Phi}_{j,k}^{-1} \frac{\iint A(w_1, s_1) \varphi_k(w, s) \theta_{atm}(w_1, s_1) \partial w_1 \partial s_1}{\iint A(w, s) \varphi_k^2(w, s) \partial w \partial s} \right) \times \left( \sum_{l=1}^N \underline{\Phi}_{j,l}^{-1} \frac{\iint A(w_2, s_2) \varphi_l(w_2, s_2) \theta_{atm}(w_2 + v_x \delta_t, s_2 + v_y \delta_t) \partial w_2 \partial s_2}{\iint A(w, s) \varphi_l^2(w, s) \partial w \partial s} \right) \right]. \quad (21)$$

The previous notation of the indexed Zernike polynomials  $Z_j$  has been redefined as  $\varphi_k$  and  $\varphi_l$  in Eq. (21), permitting the update operation, which is the means for temporally correlated evolution. By rearranging, recognizing that the expectation operation is linear, and grouping similar terms, Eq. (21) is redefined as Eq. (22):

$$R_{\bar{n}_j}(\delta_t) = \sum_{k=1}^N \sum_{l=1}^N \underline{\Phi}_{j,k}^{-1} \underline{\Phi}_{j,l}^{-1} \frac{\iint \iint A(w_1, s_1) A(w_2, s_2) \varphi_{j,k}(w_1, s_1) \varphi_{j,l}(w_2, s_2)}{\iint A(w, s) \varphi_{j,k}^2(w, s) \partial w \partial s \iint A(w, s) \varphi_{j,l}^2(w, s) \partial w \partial s} \times E[\theta_{atm}(w_1, s_1) \theta_{atm}(w_2 + v_x \delta_t, s_2 + v_y \delta_t)] \partial w_1 \partial s_1 \partial w_2 \partial s_2 \quad (22)$$

This is possible due to the first line in Eq. (21) being deterministic. Recognizing that the expectation in the second line is a correlation, Eq. (22) is redefined as Eq. (23) by a change of variables,  $\tau_x = (w_2 - w_1)$ ,  $\tau_y = (s_2 - s_1)$  and  $\partial \tau_x = \partial w_2$ ,  $\partial \tau_y = \partial s_2$ .

$$R_{\bar{n}_j}(\delta_t) = \sum_{k=1}^N \sum_{l=1}^N \underline{\Phi}_{j,k}^{-1} \underline{\Phi}_{j,l}^{-1} \frac{\iint \iint A(w_1, s_1) A(w_1 + \tau_x, s_1 + \tau_y) \varphi_{j,k}(w_1, s_1) \varphi_{j,l}(w_1 + \tau_x, s_1 + \tau_y)}{\iint A(w, s) \varphi_{j,k}^2(w, s) \partial w \partial s \iint A(w, s) \varphi_{j,l}^2(w, s) \partial w \partial s} \times R_\theta[(\tau_x + (v_x + v_b) \delta_t, \tau_y + (v_x + v_b) \delta_t)] \partial w_1 \partial s_1 \partial \tau_x \partial \tau_y \quad (23)$$

The first line of the Eq. (23) numerator is simplified as two independent correlations of Zernike polynomials with the aperture, Eq. (24) and Eq. (25):

$$F = A(w_1, s_1)\varphi_{j,k}(w_1, s_1) \quad (24)$$

$$G = A(w_1 + \tau_x, s_1 + \tau_y)\varphi_{j,l}(w_1 + \tau_x, s_1 + \tau_y) \quad (25)$$

Using Fourier transform correlation, this is subsequently redefined as the inner double integral operation  $P_{k,l}$ :

$$P_{k,l}(\tau_x, \tau_y) = \int_{-\infty}^{\infty} \int_{-\infty}^{\infty} A(w_1, s_1)\varphi_{j,k}(w_1, s_1)A(w_1 + \tau_x, s_1 + \tau_y)\varphi_{j,l}(w_1 + \tau_x, s_1 + \tau_y) \partial w_1 \partial s_1 \quad (26)$$

$P_{k,l}$ , provided in Eq. (26), is deterministic with the previously mentioned inputs, and is therefore only calculated once while computing a  $R_{\vec{n}_j}(\delta_t)$ . By defining  $P_{k,l}$  in this manner, the quadruple integral in Eq. (23) is simplified in Eq. (27) as the correlation operation is independent of the outer double integral:

$$R_{\vec{n}_j}(\delta_t) = \sum_{k=1}^N \sum_{l=1}^N \underline{\Phi}_{j,k}^{-1} \underline{\Phi}_{j,l}^{-1} \frac{\int \int P_{k,l}(\tau_x, \tau_y) R_{\theta}[(\tau_x + v_x \delta_t, \tau_y + v_x \delta_t)] \partial \tau_x \partial \tau_y}{\int \int A(w, s) \varphi_k^2(w, s) \partial w \partial s \int \int A(w, s) \varphi_l^2(w, s) \partial w \partial s}. \quad (27)$$

Unfortunately there is no method to compute the correlation between atmospheric phase screens  $R_{\theta}$  directly using Kolmogorov models for the atmosphere because  $R_{\theta}(0) \rightarrow \infty$ .

Therefore, the relationship of the phase structure to phase correlation defined by Eq. (28), is substituted in [3]:

$$D_{\vec{n}_j}(\delta_t) = 2R_{\vec{n}_j}(0) - 2R_{\vec{n}_j}(\delta_t). \quad (28)$$

Mathematical manipulation is required to use this relationship; it is necessary to rearrange Eq. (27) as well as add zero ( $+ R_{\theta}[0,0] - R_{\theta}[0,0]$ ). This substitution redefines Eq. (27) as Eq. (29), now in terms of  $D_{\vec{n}_j}(\delta_t)$  instead of  $R_{\vec{n}_j}(\delta_t)$ :

$$D_{\vec{n}_j}(\delta_t) = \sum_{k=1}^N \sum_{l=1}^N \underline{\Phi}_{j,k}^{-1} \underline{\Phi}_{j,l}^{-1} \frac{\int \int P_{k,l}(\tau_x, \tau_y) 2 \left( \begin{array}{c} R_{\theta}[0,0] - R_{\theta}[0,0] + R_{\theta}[\tau_x, \tau_y] - \\ R_{\theta}[(\tau_x + v_x \delta_t, \tau_y + v_x \delta_t)] \end{array} \right) \partial \tau_x \partial \tau_y}{\int \int A(w, s) \varphi_k^2(w, s) \partial w \partial s \int \int A(w, s) \varphi_l^2(w, s) \partial w \partial s} \quad (29)$$

By pairing the phase variances with the appropriate phase correlations, the correlation functions in Eq. (29) can be expressed in terms of a phase structure function difference:

$$D_{\vec{n}_j}(\delta_t) = \sum_{k=1}^N \sum_{l=1}^N \frac{\Phi_{-k}^{-1} \Phi_{-l}^{-1}}{\int \int A(w, s) \varphi_k^2(w, s) \partial w \partial s \int \int A(w, s) \varphi_l^2(w, s) \partial w \partial s} \int \int P_{k,l}(\tau_x, \tau_y) [D_\theta(\tau_x + v_x \delta_t, \tau_y + v_y \delta_t) - D_\theta(\tau_x, \tau_y)] \partial \tau_x \partial \tau_y. \quad (30)$$

With Eq. (30) in terms of a difference in phase structure function, Eq. (31) providing the methodology to analytically calculate  $D_\theta$ ,  $D_{\vec{n}}$  may now be solved for, and subsequently  $R_{\vec{n}}$ , by rearranging the relationship of Eq. (28),  $R_{\vec{n}} = (D_{\vec{n}} - 2)/2$ . Recall that the  $\vec{n}$  vector is zero mean and unit variance and as such,  $R_{\vec{n}}(0) = 1$ . Note that

$$D_\theta(\tau_x, \tau_y) = 6.88 \left( \frac{\tau_x^2 + \tau_y^2}{r_o^2} \right)^{5/6}. \quad (31)$$

### 3.2 Temporal Evolution of Zernike-based Phase Screens

With  $R_{\vec{n}}$  calculated for a desired number of polynomials  $N$ , and inputs  $A$ ,  $r_o$ , and wind speeds  $v_x$  &  $v_y$ , the random  $\vec{n}$  vector can be accurately updated with conditional mean, Eq. (16) and conditional variance, Eq. (17). The  $R_{\vec{n}}$  vector only needs to be generated once for each set of conditions. Subsequently, from the definition of the Zernike polynomial coefficient amplitudes, Eq. (6), the phase screen  $\phi(Sp, \theta)$  defined in Sec 2.3.2 can be temporally evolved very quickly. Note that an independent  $R_{\vec{n}}$  is required for each individual phase screen given various wind velocities. The computational requirements to generate a  $R_{\vec{n}}$  vector is a function of the number of Zernike polynomials used to simulate a phase screen. For instance, it requires less than a minute to generate  $R_{\vec{n}}$  with 128 polynomials on the computer system used to perform the analysis in this thesis. The system requires roughly 12 minutes to generate a  $R_{\vec{n}}$  with



1,024 polynomials, the amount used in all subsequent analysis. As alluded to previously, the tradeoff between this Zernike-based approach and the FFT-based approach is time. To generate the first 8 screens takes just over an hour due to the eight computations of  $R_{\vec{n}}$ . However, once the  $R_{\vec{n}}$  vectors are generated, the Zernike-based simulations described in subsequent chapters are completed in well under an hour. Inversely, the FFT-based simulations generate the initial 8 large phase screens in less than a minute, but the temporal simulations used for comparative analysis requires multiple hours to complete. This is in large part due to the computational requirements necessary to perform the sub-pixel shifts of the frozen flow model based on the Fourier shift theorem. A detailed description of implementing this sub pixel shift is provided in Sec. 5.1.2.

### 3.3 Chapter Summary

While computationally it is inefficient to regenerate the  $R_{\vec{n}}$  vector each time a simulation is performed, generating and storing a database of vectors for given input conditions permits the efficient temporal evolution of phase screens with highly accurate correlation. In contrast to the frozen-flow method in which very large phase arrays must be generated, stored, and then shifted, this Zernike-based turbulent flow method requires only the sparsely populated correlation matrix  $C$ , the correlation vector  $R_{\vec{n}}$ , and the Zernike polynomials  $Z_j$  to be stored. The update then becomes an extremely fast matrix operation which does not require the enormous amount of memory and processing time required to store and shift giant phase arrays.

## IV. Model Evaluation

This chapter's focus is the assessment of the new Zernike-based temporal model developed in the previous chapter through laboratory experiment. The first section describes the laboratory configuration within which the new model is assessed as well as the approach of extracting the observed  $r_0$  in the laboratory. Next, the comparative methods of evaluating recorded, simulated, and theoretical data are evaluated. Finally, the results of this comparison are presented.

### 4.1 Laboratory Experiment Configuration

The evaluation of this new turbulent flow model is critical to the analysis accuracy of the thesis objectives. Evaluation requires the comparison of recorded experimental data to generated simulation. The experimental data was recorded by capturing one hundred successive photos, 14 photos per second, of a pinhole point source propagated through a concentrated turbulent medium directly in front of a 2 mm limiting aperture and then focused by a lens of focal length,  $f_l = 100$  mm. A large temperature differential generated the turbulent medium. Extracting the  $r_0$  of the turbulence in this experiment is the subject of Sec. 4.2.

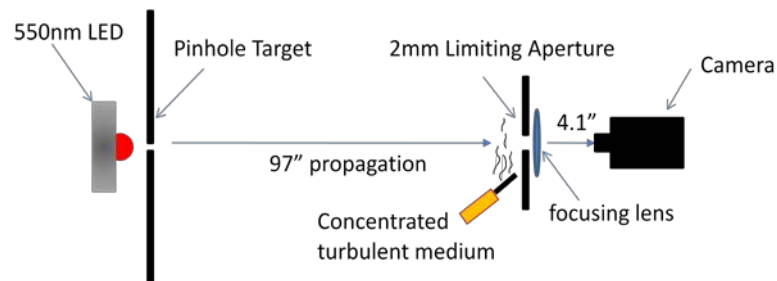


Figure 5: Experimental configuration.

### 4.1.1 Point Source

The point source is created by puncturing a piece of aluminum foil with a 22 gauge wire. The point source was illuminated by a LED with wavelength  $\lambda = 550$  nm. The backlit point source was given uniform lighting to prevent directional propagation by placing partially translucent material directly on the aluminum foil. The LED light source was then enclosed to prevent ambient light noise.

### 4.1.2 Optics

Nyquist sampling requires a sampling frequency to be greater than or equal to twice the spatial frequency cut off,  $f_s \geq 2f_c$ . The spatial frequency cut off for circular apertures is equal to the aperture diameter  $A$  divided by the wavelength times the focal length  $f_i$ , given as  $f_c = A/\lambda \cdot f_i$  [6]. Therefore Nyquist sampling is  $f_s \geq 2A/\lambda \cdot f_i$ . By rearranging and accounting for the pixel size ( $\Delta$ ) as the spatial cut off, the limiting aperture diameter  $A$  can be used to force Nyquist sampling, as provided in Eq. (32):

$$A < \frac{\lambda(f_i)}{2(\Delta)} < \frac{(550nm)(0.1042m)}{2(16\mu m)} < 2.32mm. \quad (32)$$

The focusing length was set based on a 97" propagation to the lens which has a focal length of 100 mm, or 3.937". Therefore, by the lens maker's equation,

$$\frac{1}{3.937''} = \left( \frac{1}{4.103''} + \frac{1}{97''} \right) \quad (33)$$

the focusing length  $f_L$  was set to the image distance, approximately 4.1", previously provided as 0.1042m.

The camera's CCD converts photons to charge, which is then read out serially through register operations. The camera attempts to remove the Poisson distributed

incident bias from ambient noise by subtracting the average background from the entire signal. See Fig. 6 for a physical picture of the Camera, limiting aperture, and focusing lens configuration.



**Figure 6: Camera and optics.**

#### ***4.1.3 Turbulent Medium***

Had a turbulence wheel been utilized, this analysis would be incorrectly evaluating a frozen flow approximation. Therefore a realistic concentrated turbulent medium was produced by using a soldering iron placed immediately in front of and below the limiting aperture. The iron has a rating corresponding to a tip temperature of 250 °C. This temperature differential creates a very strong turbulent medium with convective air flow. The velocity in the center of the convection  $v_c$  of the flow is given in Eq. (34) and is a function of the acceleration of gravity  $g$ , vertical distance from the surface  $l$ , ambient room temperature  $t_e$ , surface temperature  $t_s$ , and the temperature differential between the two  $d_t = t_s - t_e$  [4]:

$$v_c = 0.65 \left[ \frac{g \times l \times t_e}{(273 + d_t)} \right]^{1/2}. \quad (34)$$

Based on a 230 °C temperature difference over a 5 mm vertical distance, the  $v_c$  is calculated to be 2.68 cm/sec, which translates to just under 2 mm per captured image. This is reflected in the subsequent results section of this chapter with small yet tangible correlations in time. Based upon the long exposure OTF analysis provided in Sec. 4.3 it appears that the induced turbulent medium is Kolmogorov.

## 4.2 Extracting $r_0$

To accurately simulate the new model, the first concern is to match the laboratory configuration as closely as possible. Simulating this experiment is relatively easy given the aperture size, vertical air velocity, propagation distances, etc., except that  $r_0$  is initially unknown. Knowing  $r_0$  is crucial for accurately comparing simulation to measured data, therefore two independent approaches are utilized in its extraction.

### 4.2.1 Maximum Correlation

The first method measures the point spread function (PSF) of the raw data which is compared to theoretical PSFs as a function of  $r_0$  through a maximum correlation estimator. The mathematical representation for cross-correlation of real-valued signals across  $N$  discrete shifts is:

$$\rho(t) = \frac{1}{N} \sum_{r=0}^N \frac{(d(t) - \bar{d})(\gamma(t + \tau) - \bar{\gamma})}{\sigma_{\bar{d}}\sigma_{\bar{\gamma}}}. \quad (35)$$

Here,  $d(t)$  is the measured intensity value and  $\gamma(t + \tau)$  is the value at time  $t$  of the reference waveform shifted by time  $\tau$ , with their standard deviations,  $\sigma_{\bar{d}}$  and  $\sigma_{\bar{\gamma}}$ , to normalize the value [5]. The cross correlation value  $\rho$  reaches an absolute maximum

when the two waveforms are at an optimized alignment. Fig. 9 in Sec. 4.2.3 shows the resulting plot.

#### 4.2.2 Gerchberg-Saxton Phase Retrieval

Additionally, as a verification of the maximum correlation estimator, the recorded long exposure optical transfer function (OTF) is extracted using a Gerchberg-Saxton phase retrieval algorithm, and compared to theoretical long exposure OTFs as a function of  $r_\theta$ . The Gerchberg-Saxton algorithm iteratively uses the forward and inverse Fourier transforms to approximate the amplitudes at the source and target plane, and the intensity of the target to the source intensity. This iterative process progressively estimates, or extracts, the phase as it cycles. Figure 7 depicts the entire cycle.

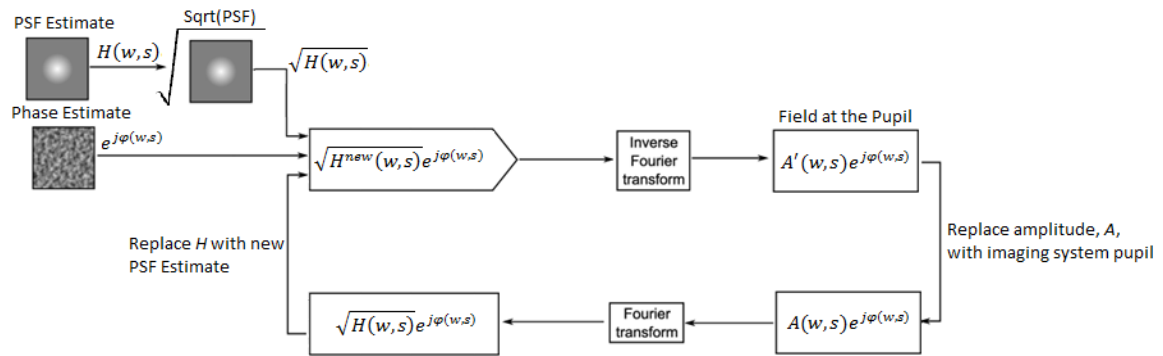


Figure 7: Gerchberg-Saxton algorithm.

The square-root of the PSF estimate  $\sqrt{H(w,s)}$  is combined with the phase estimate  $e^{j\varphi(w,s)}$  to initiate the algorithm. This iterative process updates the phase estimate as it cycles. Figure 8 shows the extracted phase from this process, both wrapped and, by a least squares error algorithm, unwrapped. The resulting mean squared error (MSE) plot between the measured and theoretical long exposure OTFs is presented in Sec. 4.2.3 Fig. 10.

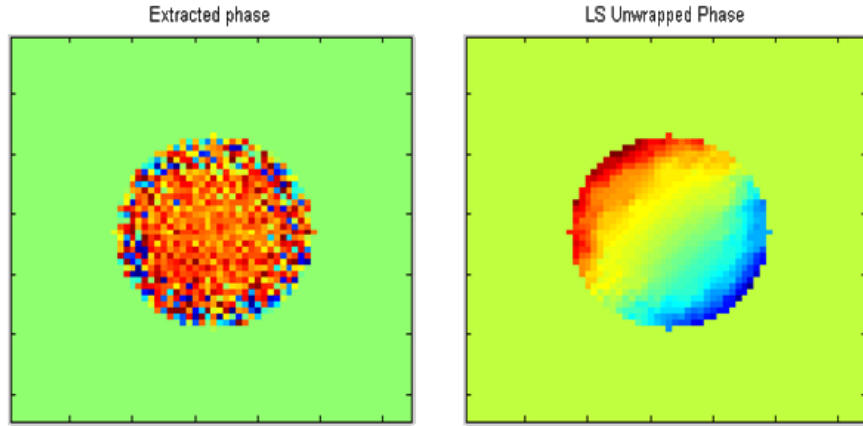


Figure 8: Phase extracted from raw data.

#### 4.2.3 Results of Extracting $r_0$

Figures 9 and 10 have maximum and minimums at 3.4 mm and 3.3 mm, respectively. With these two independent approaches of measuring  $r_0$ , it is with confidence to infer that the laboratory seeing parameter is accurately estimated as 3.4 mm. This extracted  $r_0$  allows for simulation of the frozen- and turbulent-flow models for comparative analysis. Laboratory comparison next compares the measured results with generated and theoretical results.

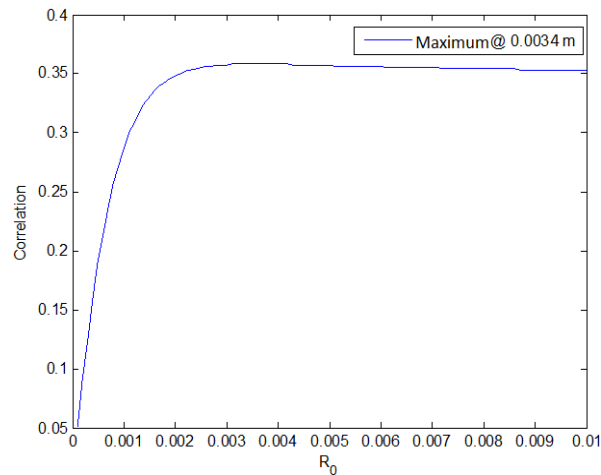
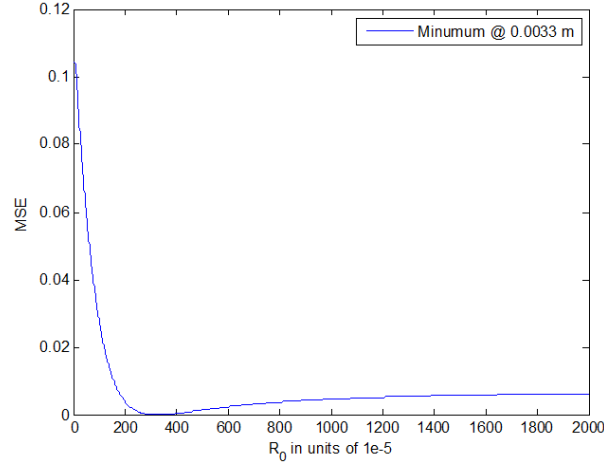


Figure 9: Maximum correlation  $r_0$  fitting.



**Figure 10: Mean squared error  $r_0$  fitting.**

Note that after reaching the maximum correlation and minimum MSE values, these graphs become asymptotic because as the respective  $r_0$  increases, the two comparison's approaches become diffraction limited.

### 4.3 Comparing Recorded, Simulated, and Theoretical Tilt Correlation in Time

With a measured  $r_0$ , [3] provides the methodology to analytically calculate the theoretical tilt correlation given input parameters  $A=2 \text{ mm}$ ,  $r_0=3.4 \text{ mm}$ , and wind velocities  $v_x = 0$  &  $v_y = 0.00192 \text{ m/s}$ . Based on the concentration of the turbulence analysis, the atmospheric phase is accepted as a thin lens approximation. The theoretical basis for calculating  $x$  and  $y$  tilt in time is provided in Eq. (36) [3]:

$$\alpha_{x,y}(t_n) = \frac{\int_{-\infty}^{\infty} \int_{-\infty}^{\infty} A(w, s) \theta_{atm}(w, s, t_n) \varphi_{x,y}(w, s)}{\int_{-\infty}^{\infty} \int_{-\infty}^{\infty} A(w, s) \varphi_{x,y}^2(w, s)}. \quad (36)$$

Tilt  $\alpha_{x,y}$  is calculated from the second and third Zernike polynomials  $\varphi_{x,y}$  which correspond to  $x$  and  $y$  tilt respectively, the aperture  $A$ , and instant draws of successive Zernike-based turbulent flow and FFT-based frozen flow phase screens  $\theta_{atm}$ . Since tilt is



zero mean [3], to calculate the temporal correlation of these tilts, it is important to recognize that the correlation of tilt in time is

$$R_{\alpha}(t_1, t_2) = E[\alpha_{x,y}(t_1), \alpha_{x,y}(t_2)]. \quad (37)$$

By Monte Carlo, an average of 100 simulations produce a Zernike- and Fourier-based generated mean tilt correlation in time. These simulations draw on the same low wind-velocity conditions calculated in Sec. 4.1.3 and the laboratory configuration of Sec. 4.1. The simulated measurements are compared to both recorded and theoretical values, all of which are presented in Table 1. The results indicate that the turbulent flow Zernike-based approach closely imitates both the recorded, and theoretical tilt correlation in time. Inversely, the frozen flow results poorly reflect both theory and recorded measurements.

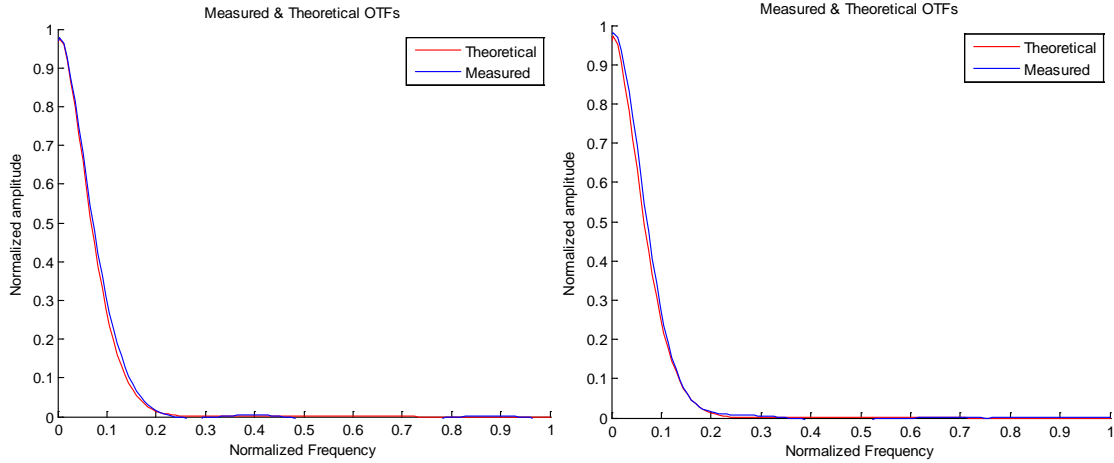
X Tilt Correlation in Time				Y Tilt Correlation in Time			
Zernike	Recorded	Theory	Fourier	Zernike	Recorded	Theory	Fourier
0.1546	0.1596	0.1489	0.8194	0.1089	0.1022	0.1080	0.0512

Table 1: Tilt correlation in time

This table is divided left to right by the observed  $x$  and  $y$  tilt correlations in time. The  $x$  direction is horizontal, and the  $y$  direction is vertical while viewing from the direction of propagation. Each section is further divided by the: *Zernike*-based turbulent flow simulation, laboratory measured and *Recorded*, analytically calculated *Theory* values, and *Fourier*-based frozen flow modeled tilt correlations in time.

In addition to these findings on temporal tilt correlation in time, including 1,024 Zernike polynomials provides comparatively equivalent high special frequency content as that of Fourier-based approaches. This is evidenced by the simulated long exposure OTF of this new turbulent flow model being equivalent to the OTF of standard frozen flow models [11]. This related technical paper shows that with using a mere 400 Zernike

polynomials acceptably mimics the frequency content of the long exposure OTF as evidenced by Fig. 11 which provides MSE values of  $1.14\text{E-}4$  and  $9.08\text{E-}5$  between the theoretical and the Fourier and Zernike OTFs, respectively.



**Figure 11: Theoretical OTF compared to Fourier (left) & Zernike (right).**

#### 4.4 Chapter Summary

In summary, comparison of the Zernike-based temporally evolving screen is accomplished by pairing a simulated thin lens approximation with the parameters as described in Sec. 4.1. The laboratory configuration circumvents the need to account for multiple layers of atmospheric turbulence and high wind speeds, which frozen flow approximations already accurately model. Through this laboratory experiment it is shown that the new turbulent flow Zernike-based model provides better tilt correlation in time than the frozen flow approximation does. This finding is the result of Monte Carlo analysis which compares theoretical, recorded, and the two approaches to simulate values of tilt correlation. Further testing is required to verify higher order aberrations are correctly simulated since the laboratory environment was limited to an  $A / r_0 \leq 1$ .

## V. Simulation Analysis and Results

This chapter discusses the methodology for accomplishing the objectives outlined in Sec. 1.2. Based upon simulated phase screen analysis, this chapter discusses atmospheric attributes and related approximations, as well as how both the Zernike- and FFT-based phase screens are appropriately simulated. Additionally, the approach for calculating modulation efficiency is included. Finally, this chapter provides the analytical results for both approaches of atmospheric impacts on long pulse LADAR beams in the form of mixing efficiencies.

### 5.1 Simulation Environment

In order to analyze what effects the atmosphere has upon mixing efficiency as the LADAR pulse length changes, propagation through atmospheric turbulence must be accurately simulated. The 3.67 m class AEOS telescope at the AMOS on Mt. Haleakalā is the intended observatory to utilize the ISAL capability. Therefore utilizing the basic parameters of the AEOS will best address the objectives of this thesis. Note that the AO system is not directly modeled into the simulation because the AO cannot account for the temporal effects as previously discussed. However, it is assumed that the AO system effectively corrects wavefront error at time  $t = 0$ , or at the initiation of each illumination pulse.

Two additional and forefront simplifications of this simulation are the absence of anisoplanatic effects and scintillation noise. Anisoplanatic effects are of primary concern while viewing objects large enough for light from the target to propagate through different parts of the atmosphere to the observatory. For example, looking at the moon

versus looking at a distant star. Due to the significant distance and a relative point source target anisoplanatic effects may be ignored for this analysis, which greatly simplifies the simulation. Secondly, ignoring scintillation noise is a conscious calculation. The concentration of this analysis is to simulate and analyze idealistic conditions so that research efforts will better understand mixing efficiencies. By ignoring scintillation effects, this analysis provides a baseline for such understanding.

### 5.1.1 Atmosphere

Atmospheric turbulence is represented by phase screens generated using two methods: the turbulent flow model described in Ch. III and then compared in Ch. IV, and the frozen flow model generated by Sec. 2.3.1 and evolved by Sec. 5.1.2. Eight independent screens are generated representing thin lens approximations of the eight respective atmospheric regions shown in Fig. 12.

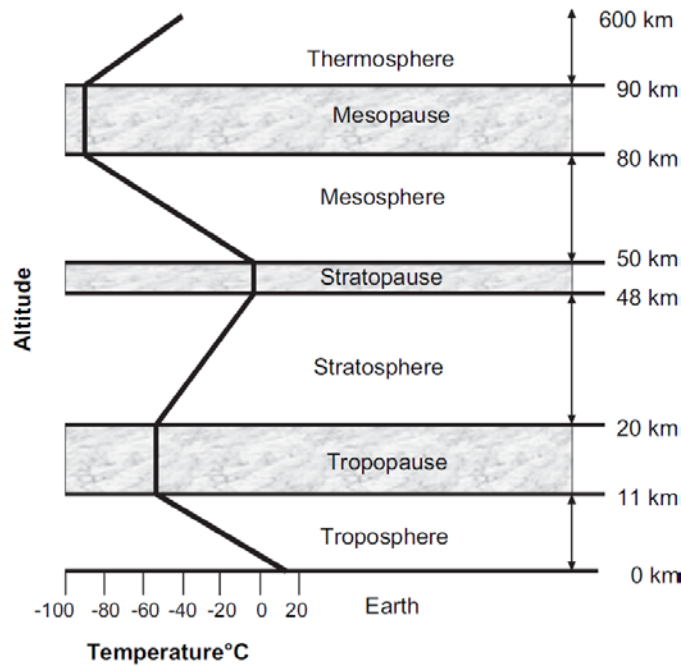


Figure 12: Atmosphere's structure.

These phase screen representations of atmospheric regions are the: Thermosphere, Mesopause, Mesosphere, Stratopause, Stratosphere, Tropopause, and Troposphere, and an eighth screen is dedicated to the fast flowing, narrow current of the Jet Stream; which is located near the transition between the Troposphere and Tropopause [1]. The FFT-based frozen flow approach is simulated for comparative analysis to the Zernike-based turbulent flow approach, and the results of this experiment are presented in Sec. 5.2.2.

As a consequence of ignoring anisoplanatism, the atmospheric phase screens do not require screen to screen propagation. As such, the eight independently evolving Zernike-based screens depicted in Fig. 13 and FFT-based screens shown in Fig. 14 are summed together, the results of which are presented in Fig. 15 and Fig. 16, respectively. By this summation a single far field propagation is easily performed for each time sample effectively modeling turbulence as being directly in front of the telescope. Due to the 40 Mm propagation the Fraunhofer diffraction condition in Eq. (38) is easily satisfied, i.e.,

$$z \gg \frac{k(\xi^2 + \eta^2)_{max}}{2} = 4 \times 10^7 m \gg 5.712 \times 10^6 m \quad (38)$$

where  $z$  is the 40Mm distance propagated,  $k$  is the wave number,  $2\pi/\lambda$  where  $\lambda$  is 550 nm, and  $(\xi, \eta)$  are the Cartesian coordinates in the parallel plane in the  $x$  and  $y$  directions. The variables  $\xi^2$  and  $\eta^2$  denote the distance in the  $x$  and  $y$  directions. With this condition met, a simple two-dimensional FFT of the GEO target may be performed, accurately modeling a Fraunhofer propagation [7].

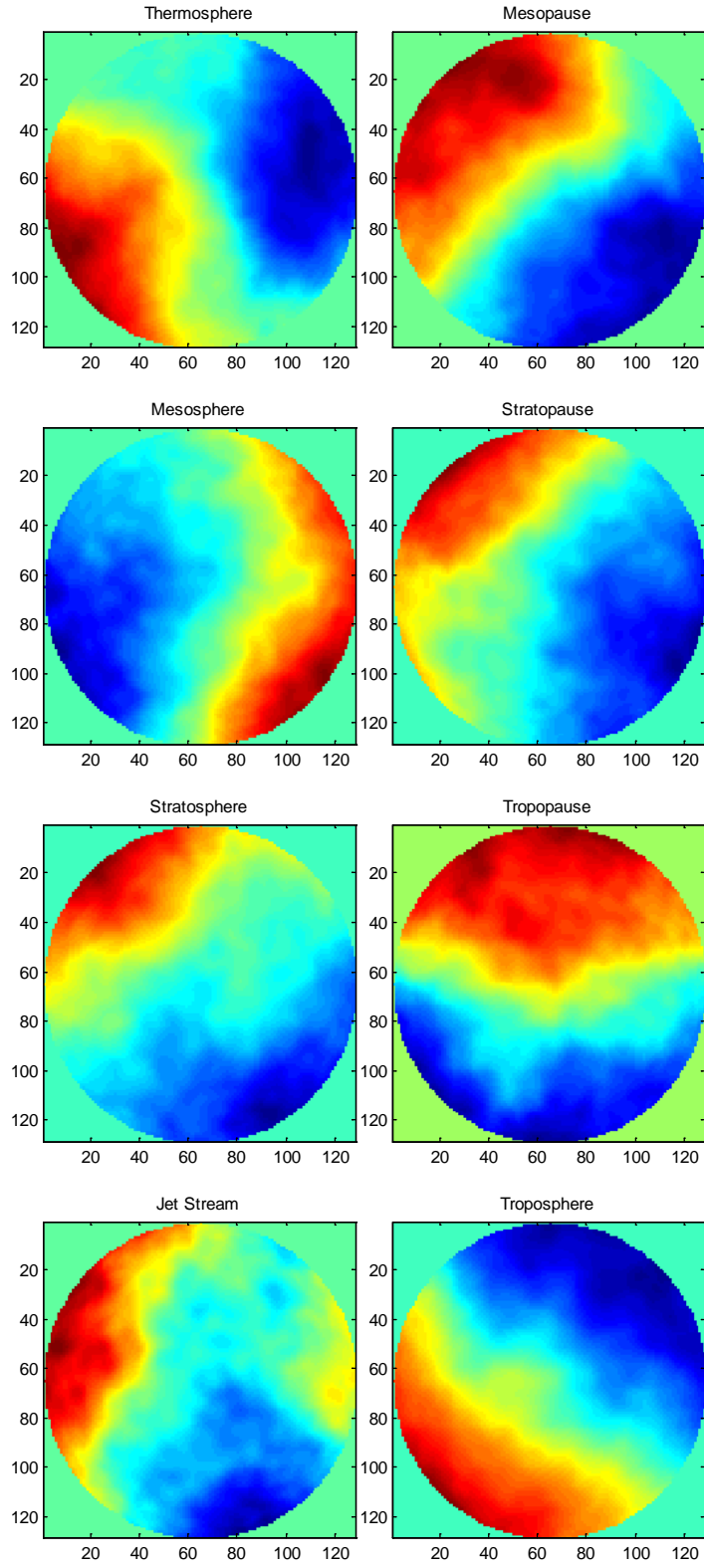


**Figure 13: Zernike phase screens representing atmospheric layers.**

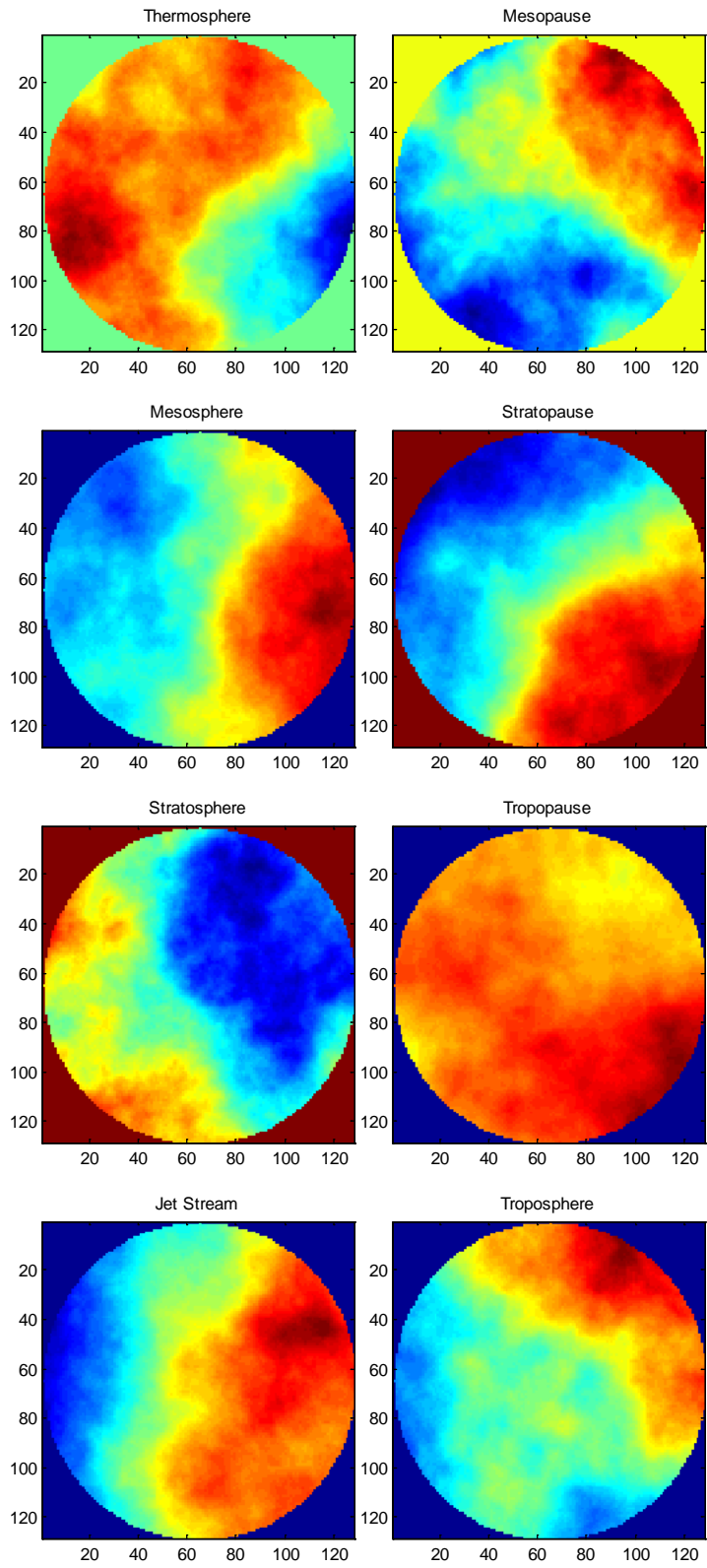


**Figure 14: FFT phase screens representing atmospheric layers.**

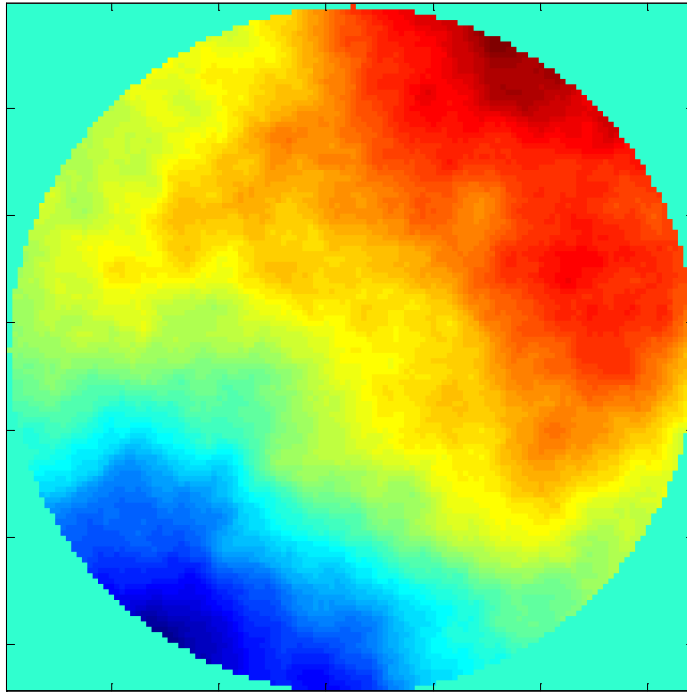


Figure 15: Total Zernike-based phase, representing 8 atmospheric layers.

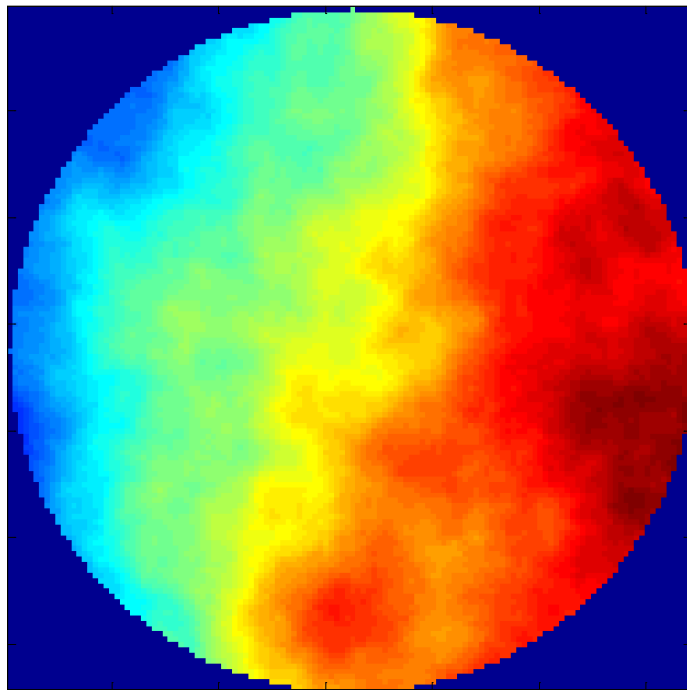


Figure 16: Total FFT-based phase, representing 8 atmospheric layers.



### 5.1.2 Sub Pixel Shifting

As previously stated, FFT-based screens are temporally evolved by the frozen flow approximation. However due to the time scales of ISAL, winds in excess of 30 m/sec translate to simulated screen shifts significantly less than a single pixel. If this analysis were simplified, and these fractional shifts simply rounded, the screens would not move. Therefore, to accomplish a non-discrete shift in a discrete environment the very large FFT screens are shifted using the Fourier shift theorem. This theorem states that if  $\mathcal{F}\{g(x,y)\} = G(f_x, f_y)$ , then with real-valued constants  $a$  and  $b$

$$\mathcal{F}\{g(x - a, y - b)\} = G(f_x, f_y)e^{-j2\pi(f_x a, f_y b)}. \quad (39)$$

In essence, the shift in the spatial domain is completed by introducing a linear phase shift in the frequency domain. This linear phase shift  $e^{-j2\pi(f_x a, f_y b)}$  is calculated by Euler's formula. For instance, a 13 m/sec  $x$ -directional wind velocity translates to a sub pixel shift according to

$$X_{shift} = \frac{(13 \text{ m/sec})(\Delta_t)}{(A/N)} = 0.0145, \quad (40)$$

where  $\Delta_t$  is 1  $\mu$ sec (the time between samples),  $A$  is 3.67 m (the primary aperture diameter), and  $N$  is 4,096 (the number of pixels on the phase screen in the  $x$  direction).

This fraction is fed into Euler's formula

$$e^{jx_{shift}} = (\cos x_{shift} + j \sin x_{shift}), \quad (41)$$

which is then factored into the  $f_x$  and  $f_y$  of the Fourier shift theorem for  $x$  and  $y$  directional winds respectively. This ensures that the spatial domain of the original screen remains unaltered, but simply shifted.

### ***5.1.3 Coherent Illumination Beam***

The ISAL beam will be utilizing a chirped waveform; however this is modeled into the simulation environment with a rectangle function waveform. The GEO space object is modeled as a single pixel in the source plane, illuminated by this unit amplitude rectangle waveform of varying length. This analysis permits the ISAL beam length to vary from 10  $\mu\text{sec}$  to 100  $\mu\text{sec}$ , by 1  $\mu\text{sec}$  intervals, for a total of 91 different pulse lengths. The modulation efficiency is calculated by the total intensity received per pulse, Eq. (46).

### ***5.1.4 System Integration***

The simulation is built into `Matlab`<sup>®</sup> in the following manner. First the constant variables such as aperture diameter  $A$ , Fried's constant  $r_0$ , sampling sizes for the aperture and receiver planes are set, and the first 1,024 Zernike polynomials are loaded. From the Zernike polynomials and the methodology detailed in Ch. II, the covariance matrix  $C$  is generated. Random wind velocities for each atmospheric layer are randomly populated from a uniform distribution of -35 m/s to +35 m/s wind speeds in the  $x$  and  $y$  directions, permitting 360° of directional wind of randomly varying intensity for each independent atmospheric layer.

These parameters are then fed into the temporal correlation algorithm developed in Ch. III, providing the correlation vector  $R_{\vec{n}}(\delta_t)$  for evolving the eight Zernike-based atmospheric phase screens. Transversely, these random wind speeds feed into the frozen flow approach which equate to the sub-pixel shifts detailed in Sec. 5.1.2. The Zernike phase screens are then randomly generated by Eq. (5) and Eq. (6), the FFT screens are

generated by the approach described in Sec. 2.3.1, and then both are evolved in their respective manner.

These eight independently generated, evolving and flowing screens are then summed over the third dimension for each time interval, where  $\delta_t = 1 \mu\text{sec}$  since anisoplanatic effects are ignored. A single FFT propagation is performed to the aperture through that instance of the total atmosphere. Then a second FFT propagation is performed from the aperture to the receiver plane, where the test and reference beams are combined as discussed in Sec. 2.4 and are shown in Fig. 17 and Fig. 18. The raw images on the left of these figures are the total test beam image in the receiver plane; whereas, the combined images on the right are the test and reference beams combined. These beams are used to measure the mixing efficiencies as calculated in Sec 5.2. It is visually apparent that this method of heterodyne detection greatly increases the SNR.

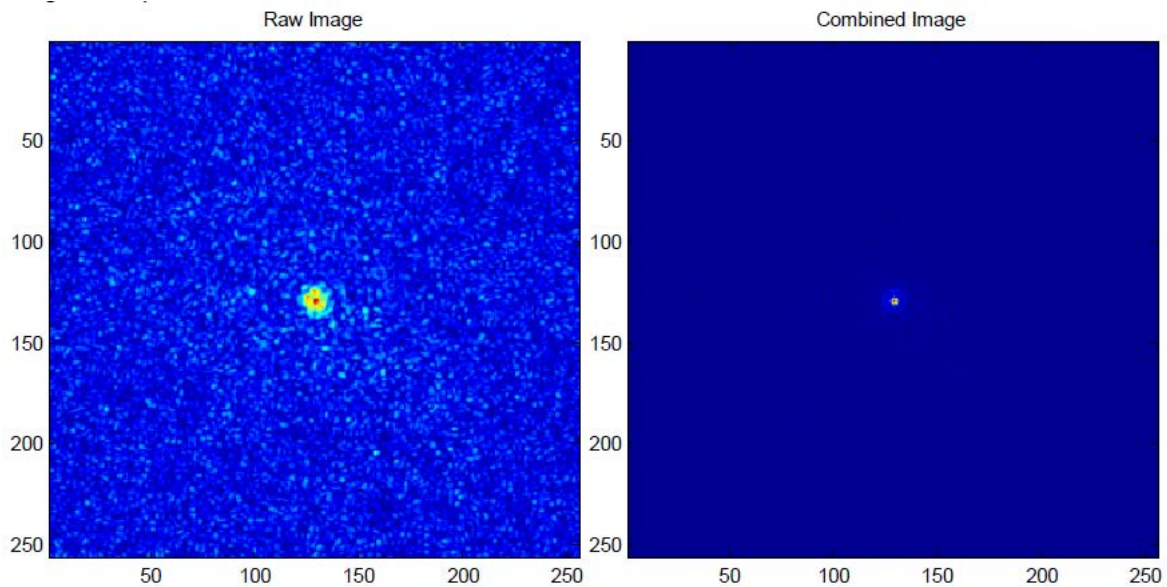


**Figure 17: Atmospheric effects over 10  $\mu\text{sec}$  pulse.**

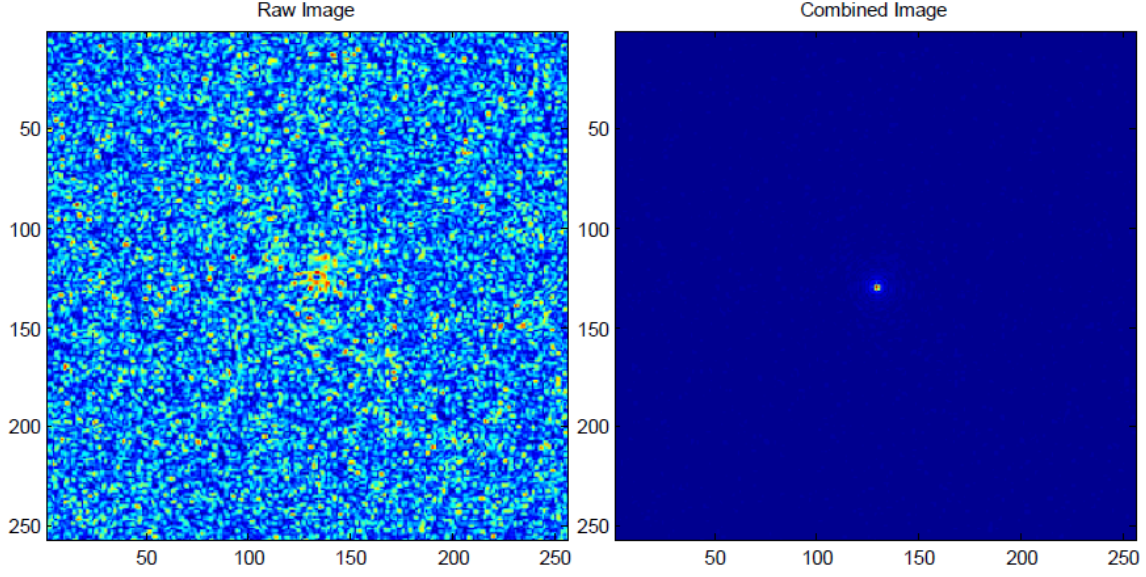


Figure 18: Atmospheric effects over 100  $\mu$ sec pulse.

## 5.2 Modulation Efficiency as the Pulse Length Varies

Building on the introduction of modulation efficiency provided in Sec. 2.4, the total intensity  $I$  in both beams is provided in Eq. (42) and Eq. (43), of which  $g_{control}$  and  $g_{test}$  are the resulting fields in the receiver plane with coordinates  $(x,y)$ :

$$I_{control} = \sum_{x=1}^N \sum_{y=1}^N |g_{control}(x,y) + g_{control}(x,y)|^2 \quad (42)$$

$$I_{test} = \sum_{x=1}^N \sum_{y=1}^N |g_{test}(x,y) + g_{control}(x,y)|^2. \quad (43)$$

The  $g_{beam}$ 's are calculated by Eq. (44) and Eq. (45), the FFT of the image in the aperture plane  $P_A$ , multiplied by the aperture  $A$ , and the complex phase at the aperture plane:

$$g_{Test} = \mathcal{F}\{P_A \times A \times e^{j\theta_{atm\Delta}}\} \quad (44)$$

$$g_{Control} = \mathcal{F}\{P_A \times A \times e^{j0}\} \quad (45)$$

Note that for the control beam, atmospheric perturbations  $\theta_{atm\Delta}$ , is a zero matrix because it is assumed that the control beam used to boost the SNR ratio does not incur any phase

delays or aberrations within its delay loop. The test beam  $\theta_{atm\Delta}$  is the total atmospheric change for a given pulse length as previously described. The ratio of these total energies, provided in Eq. (46), provides the modulation efficiency  $M$ :

$$M = \frac{I_{(test)} - (I_{(control)}/2)}{(I_{(control)}/2)}. \quad (46)$$

The approach to this ratio isolates the modulation efficiency from the total intensity.

### ***5.2.1 Total Atmospheric Change***

The total atmospheric change  $\theta_{atm\Delta}$  varies as the pulse length varies. For shorter pulse lengths, the atmosphere has less time to change, thus the impacts the atmosphere has on any light propagating through it will understandably be less. Of particular interest is the nature in which the two approaches vary as they evolve during the pulse length as shown in Fig. 19. The image on the top is the Zernike-based approach whereas the bottom is the FFT-based approach. Both images are the simulated total atmospheric change during a 100  $\mu$ sec pulse. Recall that it is assumed the AEOS AO system corrects for the atmospheric wavefront at time  $t = 0$ .

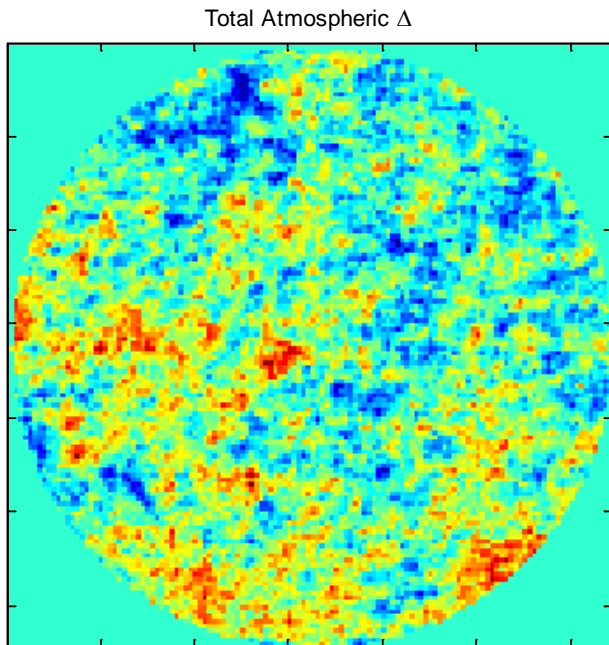
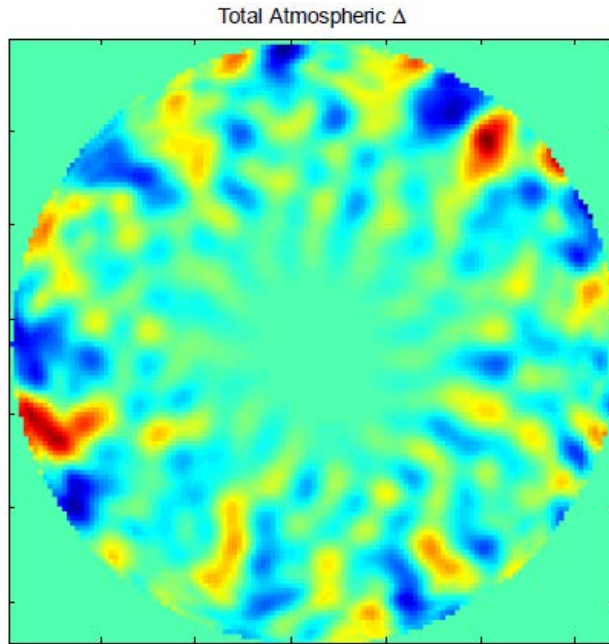


**Figure 19: Total atmospheric change in Zernike-based (top) and FFT-based (bottom).**

Of additional concern are the significant differences in amplitude between the two approaches. Note the  $z$ -axis scale in units of radians, see Figures 20 and 21.

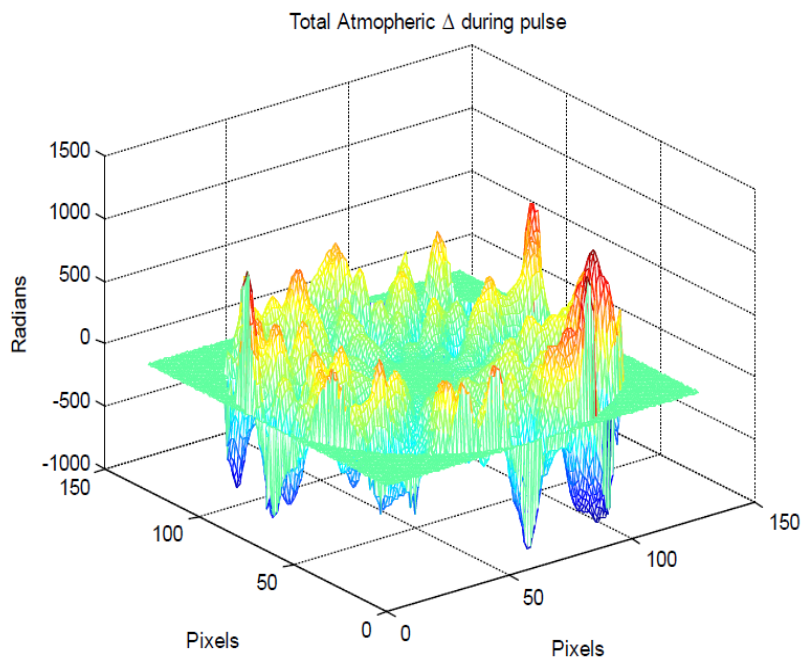
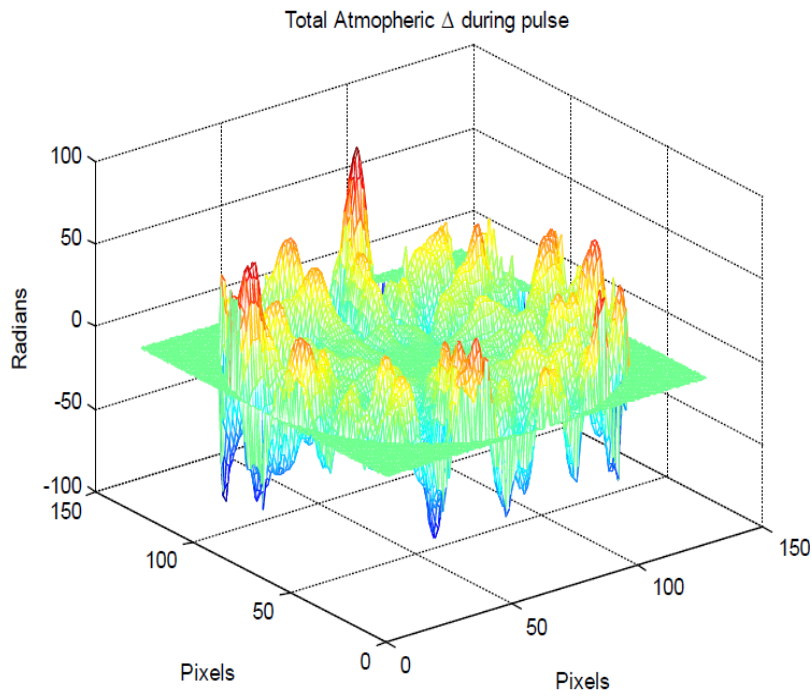


Figure 20: Zernike-based  $\theta_{atm\Delta}$  over 10  $\mu\text{sec}$  pulse (top) and 100  $\mu\text{sec}$  pulse (bottom).

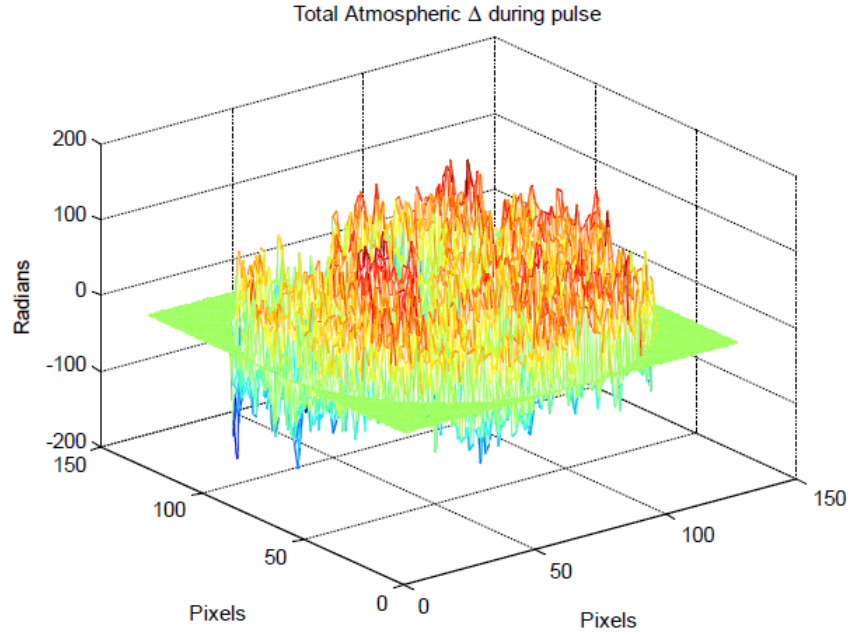
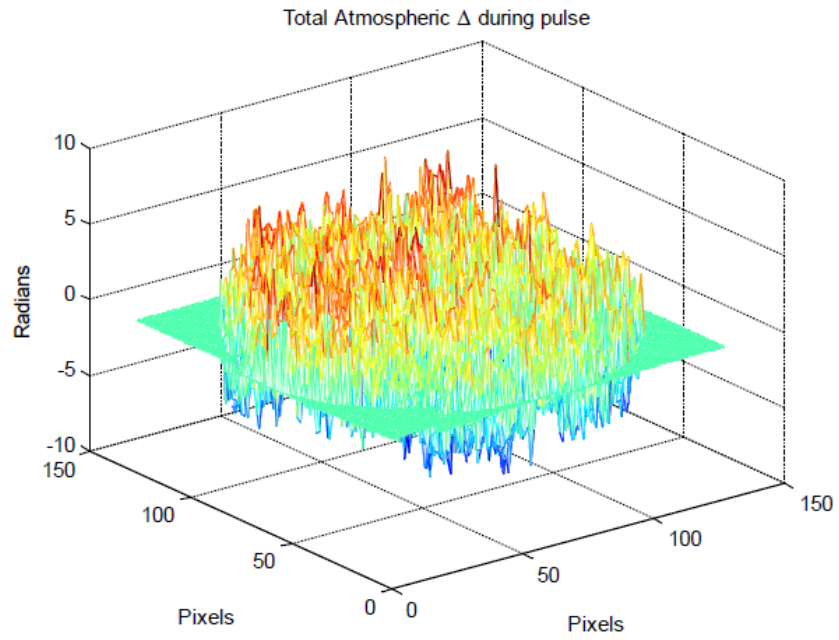


Figure 21: FFT- based  $\theta_{atm\Delta}$  over  $10 \mu\text{sec}$  pulse (top) and  $100 \mu\text{sec}$  pulse (bottom).



The  $z$  axis scales from the mesh plots of these two figures indicate that between the two approaches, the total atmospheric change is considerably less for the frozen flow method than that of the turbulent flow. It is expected that large amount of high frequency content in Fig. 19 and Fig. 21 is largely due to the sub-pixel shifting method utilized.

### 5.2.2 Mixing Efficiency Results

The differences in amplitude of atmospheric change are confirmed and validated by Monte Carlo experiment of the simulation process of Sec. 5.1. Appendix A provides the full set of captured mixing efficiencies for the Zernike results, and Appendix B provides the corresponding FFT results. The mean values of the captured data are plotted in Fig. 22 and represent the average mixing efficiency values.

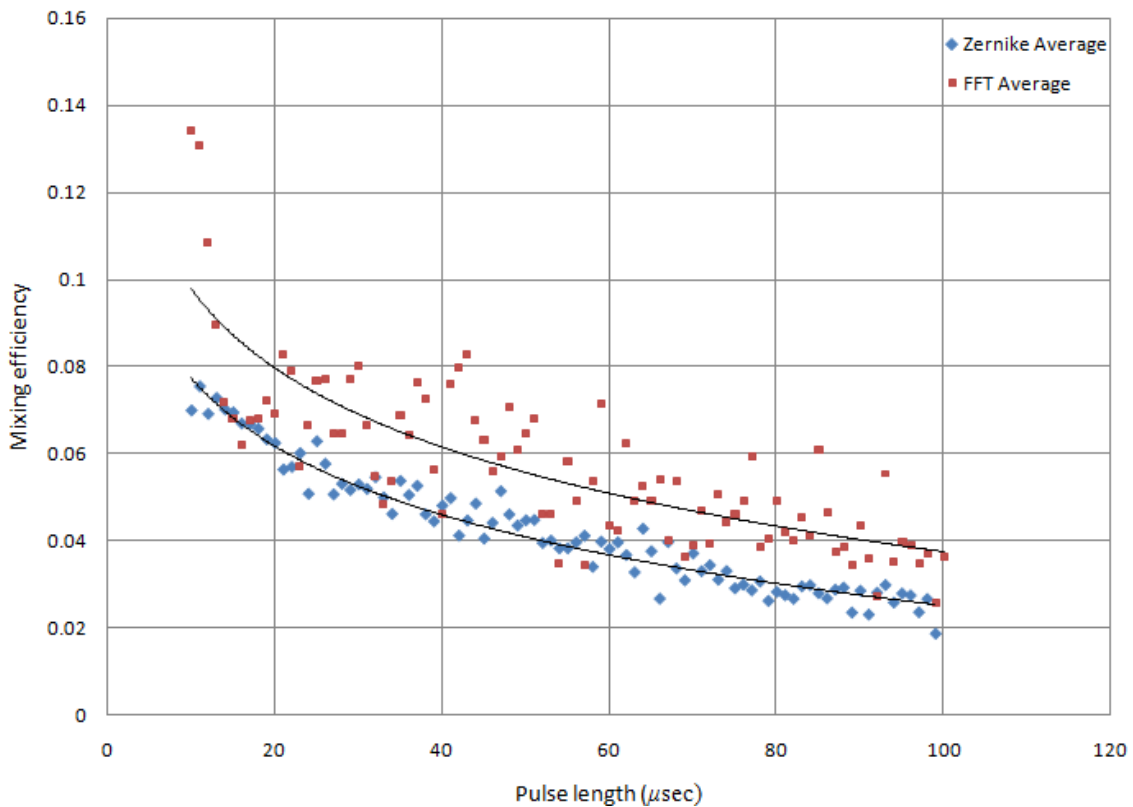


**Figure 22: Average mixing efficiency with logarithmic trend lines.**

Two items are readily apparent from this scatter plot: the FFT based approach has a much higher standard deviation from its trend and is on average much higher than the Zernike based results. The  $\sigma^2$  for the FFT method is 2.74% and 0.35% for the Zernike based method. Additionally, the frozen flow approximation mean is on average 47% higher than what the turbulent flow model predictions. This indicates that if the ISAL program limits its investigation of mixing efficiency to a frozen flow approximation, they will potentially be over estimating mixing efficiencies by roughly 50 percent.

### **5.3 Chapter Summary**

This chapter addressed the approach to the simulation used to meet the objectives set in Sec. 1.2. It built upon the theory and validation of Ch.'s III and IV, respectively, and showed that as the pulse length extends, the modulation efficiency is degraded for both the FFT and the Zernike approaches. Of particular significance, the predicted average values of the frozen flow approximation results are greater than expected. This chapter showed that for small time scales the atmosphere can in fact significantly evolve, reaffirming the understanding that the atmosphere does not in fact adhere to frozen flow. Additionally, it was shown that the new Zernike model provides more tightly fitting predictions given the measured standard deviation of the mean mixing efficiencies between the two approaches.

## VI. Conclusions and Recommendations

This chapter summarizes the efforts of this research and the resulting findings. Particular contributions are highlighted and the challenges are detailed. In addition, recommendations for future work are included to help further the research of turbulent flow, temporally evolving phase-screen generation.

### 6.1 Summary

As discussed in Ch. 1, the objective of this research has been to evaluate the atmospheric effects on long pulse LADAR beams. To meet this objective, this thesis predominately focused on the development, comparison, and utilization of an entirely new temporally evolving Zernike-based turbulent flow phase screen generation model. Building on the understanding of generating independent Zernike-based phase screens established in Ch. II, the temporal model was developed by expanding a random walk algorithm. This random walk algorithm was previously applied to atmospheric tilt [3], and Ch. III expanded the algorithm to include any  $N$  number of Zernike polynomials. This model was then validated through laboratory experiment in Ch. IV and used to provide the analysis of the objectives listed in Sec. 1.2. The simulation application of the mathematics behind the temporal aspect to Zernike-based phase screens was by far the most difficult aspect of this research effort. The analysis of the objectives was completed in Ch. V and compared to FFT-based frozen flow analysis. It was determined that as the pulse length elongates, the mixing efficiency declines. Furthermore, it was shown that the frozen flow approach has a higher standard deviation from its trend line, while the turbulent flow approach provided much tighter fitting data points. The

assumptions made at the initiation of this research effort, such as the limitation of the frozen flow approximation to relatively small atmospheric effects, were confirmed.

## 6.2 Conclusions of Research

It was determined that as the pulse length extends, mixing efficiencies decline. Based upon the Zernike results, a roughly 8% efficiency at 10  $\mu$ sec and 2% mixing efficiency at 100  $\mu$ sec closely follows a logarithmic decline. Similar in general decline, but strikingly different in noise levels, the frozen flow approach potentially overestimated the mixing efficiencies of the new turbulent flow model. Additionally the turbulent flow model was validated through laboratory experiment. The experiment captured images of a point source with a concentrated turbulent medium directly in front of the limiting aperture, and through a PSF likelihood maximization algorithm and Gerchberg-Saxton phase retrieval algorithm, extracted realistic, turbulent, temporally evolving phase. Modeling the laboratory conditions into simulation and then applying both the new Zernike-based turbulent flow model and the FFT-based frozen flow model, it was determined that the turbulent flow outperformed the frozen flow in accurately predicting tilt in time. Through previous and directly related analysis [11], it was shown that this new Zernike approach outperforms the frozen flow approximation in predicting atmospheric effects in temporal analysis.

## 6.3 Significance of Research

As stated previously, the true significance of this research was the development of the new turbulent flow model of atmospheric phase screen generation and its comparison. This new model outperformed the frozen flow approximation in comparing both

laboratory results and theoretical tilt correlations in time. With these results, a baseline may be struck for future efforts within the ISAL program. Furthermore, the new model may be applied to an assortment of applications in Space Situational Awareness (SSA), Defense Advanced Research Programs Agency (DARPA), and deep space surveillance, to name a few. The predominate application to the relevant programs directly involves more accurately estimating temporal effects when imaging through the atmosphere. The novelty of this new model's approach is of considerable significance, as currently there is no other temporal evolution phase screen generation model that is not limited to frozen flow approximations, much less any such model that has been validated as this one has.

#### **6.4 Recommendations for Future Research**

The overarching question in response to proposing this new approach to phase screen generation has been, "Can this methodology be applied to Fourier-based methods of phase screen generation?" The answer is yes. However, the number of calculations for correct correlation will balloon to an  $N^2$  number of calculations for individual pixel updates. Instead of building on the inherent correlation between Zernike's, it is expected that the pixel to pixel correlation update be rooted within the power spectrum used for generating the individual FFT-based phase screens. Instead of generating an  $R_n(\delta_i)$  vector, an  $R_n(\delta_i)$  matrix must be generated for each set of given atmospheric conditions, observatory parameters, etc. This correlation matrix would then feed into the conditional mean and conditional variance update matrices. Finally, in similar fashion to the considerably easier simulation described in the previous chapters, the correlation matrix can be paired with FFT based phase screen generation, and each pixel could then be

updated. The theoretical mathematics to accomplish this is not overly difficult and will likely follow a very similar approach to that of Ch. III. However, the difficulty in adapting such math into simulation space is known to be considerable.

## **6.5 Chapter Summary**

This chapter summarized the activities of this research and the results obtained. Accomplishing the objectives presented in Ch. I supported the hypothesis that as the LADAR pulse elongates, the atmospheric effects increase. This degradation in mixing efficiency appeared to follow a logarithmic decline. The challenges overcome and significant contributions were also highlighted. Finally, this chapter outlined the expected approach to developing a Fourier-based temporal model not limited to frozen flow approximations.

## Appendix A – Zernike-based Mixing efficiency

<b>10 <math>\mu</math>sec</b>	<b>11 <math>\mu</math>sec</b>	<b>12 <math>\mu</math>sec</b>	<b>13 <math>\mu</math>sec</b>	<b>14 <math>\mu</math>sec</b>	<b>15 <math>\mu</math>sec</b>	<b>16 <math>\mu</math>sec</b>	<b>17 <math>\mu</math>sec</b>	<b>18 <math>\mu</math>sec</b>	<b>19 <math>\mu</math>sec</b>
0.0708	0.0708	0.0731	0.0599	0.0709	0.0629	0.055	0.07	0.0791	0.0612
0.0604	0.064	0.0817	0.0646	0.0718	0.0693	0.0683	0.0599	0.0691	0.0707
0.0701	0.095	0.0623	0.0655	0.0602	0.0703	0.0679	0.0656	0.0594	0.0494
0.0789	0.0734	0.0653	0.0872	0.0652	0.0682	0.0709	0.0669	0.0622	0.0664
0.0689	0.0736	0.0627	0.0862	0.0823	0.0761	0.0721	0.071	0.0584	0.0683
<b>0.06982</b>	<b>0.07536</b>	<b>0.06902</b>	<b>0.07268</b>	<b>0.07008</b>	<b>0.06936</b>	<b>0.06684</b>	<b>0.06668</b>	<b>0.06564</b>	<b>0.0632</b>
<b>20 <math>\mu</math>sec</b>	<b>21 <math>\mu</math>sec</b>	<b>22 <math>\mu</math>sec</b>	<b>23 <math>\mu</math>sec</b>	<b>24 <math>\mu</math>sec</b>	<b>25 <math>\mu</math>sec</b>	<b>26 <math>\mu</math>sec</b>	<b>27 <math>\mu</math>sec</b>	<b>28 <math>\mu</math>sec</b>	<b>29 <math>\mu</math>sec</b>
0.0619	0.0518	0.0544	0.0533	0.054	0.0679	0.0579	0.0521	0.0447	0.0533
0.0691	0.0582	0.0516	0.0664	0.0406	0.0617	0.0463	0.0453	0.055	0.0443
0.0558	0.0555	0.0579	0.0594	0.0473	0.0685	0.0584	0.0565	0.0663	0.0441
0.0653	0.0566	0.0636	0.0568	0.0479	0.046	0.0693	0.0505	0.0535	0.0673
0.0596	0.0592	0.0568	0.0642	0.0637	0.0697	0.056	0.0485	0.0454	0.0488
<b>0.06234</b>	<b>0.05626</b>	<b>0.05686</b>	<b>0.06002</b>	<b>0.0507</b>	<b>0.06276</b>	<b>0.05758</b>	<b>0.05058</b>	<b>0.05298</b>	<b>0.05156</b>
<b>30 <math>\mu</math>sec</b>	<b>31 <math>\mu</math>sec</b>	<b>32 <math>\mu</math>sec</b>	<b>33 <math>\mu</math>sec</b>	<b>34 <math>\mu</math>sec</b>	<b>35 <math>\mu</math>sec</b>	<b>36 <math>\mu</math>sec</b>	<b>37 <math>\mu</math>sec</b>	<b>38 <math>\mu</math>sec</b>	<b>39 <math>\mu</math>sec</b>
0.0547	0.0493	0.0506	0.0459	0.0387	0.0564	0.0472	0.0553	0.0465	0.0404
0.0518	0.0521	0.0468	0.0545	0.0599	0.0623	0.0558	0.0526	0.0536	0.0528
0.0494	0.0582	0.0625	0.0587	0.0435	0.0426	0.0351	0.0557	0.0385	0.039
0.0573	0.0595	0.0522	0.0466	0.0495	0.0466	0.0497	0.0564	0.0382	0.0351
0.051	0.04	0.0605	0.0437	0.0388	0.0604	0.0643	0.0427	0.0532	0.0546
<b>0.05284</b>	<b>0.05182</b>	<b>0.05452</b>	<b>0.04988</b>	<b>0.04608</b>	<b>0.05366</b>	<b>0.05042</b>	<b>0.05254</b>	<b>0.046</b>	<b>0.04438</b>
<b>40 <math>\mu</math>sec</b>	<b>41 <math>\mu</math>sec</b>	<b>42 <math>\mu</math>sec</b>	<b>43 <math>\mu</math>sec</b>	<b>44 <math>\mu</math>sec</b>	<b>45 <math>\mu</math>sec</b>	<b>46 <math>\mu</math>sec</b>	<b>47 <math>\mu</math>sec</b>	<b>48 <math>\mu</math>sec</b>	<b>49 <math>\mu</math>sec</b>
0.05	0.0438	0.0456	0.0487	0.0417	0.0491	0.0389	0.0486	0.0587	0.0403
0.0535	0.0547	0.0335	0.0385	0.0393	0.0357	0.035	0.0537	0.0373	0.0533
0.0418	0.0535	0.0438	0.0479	0.0435	0.0413	0.0499	0.047	0.0449	0.0474
0.0505	0.0337	0.0451	0.0515	0.0604	0.0395	0.0453	0.0435	0.0485	0.0329
0.0442	0.0628	0.0375	0.0363	0.0574	0.0365	0.0511	0.0637	0.0404	0.0432
<b>0.048</b>	<b>0.0497</b>	<b>0.0411</b>	<b>0.04458</b>	<b>0.04846</b>	<b>0.04042</b>	<b>0.04404</b>	<b>0.0513</b>	<b>0.04596</b>	<b>0.04342</b>
<b>50 <math>\mu</math>sec</b>	<b>51 <math>\mu</math>sec</b>	<b>52 <math>\mu</math>sec</b>	<b>53 <math>\mu</math>sec</b>	<b>54 <math>\mu</math>sec</b>	<b>55 <math>\mu</math>sec</b>	<b>56 <math>\mu</math>sec</b>	<b>57 <math>\mu</math>sec</b>	<b>58 <math>\mu</math>sec</b>	<b>59 <math>\mu</math>sec</b>
0.0332	0.0474	0.0362	0.0435	0.0405	0.0377	0.0331	0.0388	0.0272	0.0454
0.0418	0.0379	0.0497	0.0383	0.0383	0.0395	0.0362	0.0444	0.0239	0.0391
0.0488	0.0397	0.039	0.0416	0.0364	0.0376	0.0457	0.0423	0.0408	0.0345

0.0378	0.0467	0.0291	0.0409	0.0345	0.0355	0.0495	0.0431	0.0328	0.0289
0.0615	0.0518	0.0431	0.0355	0.0413	0.0407	0.0333	0.0367	0.045	0.0507
<b>0.04462</b>	<b>0.0447</b>	<b>0.03942</b>	<b>0.03996</b>	<b>0.0382</b>	<b>0.0382</b>	<b>0.03956</b>	<b>0.04106</b>	<b>0.03394</b>	<b>0.03972</b>
<i>60 μsec</i>	<i>61 μsec</i>	<i>62 μsec</i>	<i>63 μsec</i>	<i>64 μsec</i>	<i>65 μsec</i>	<i>66 μsec</i>	<i>67 μsec</i>	<i>68 μsec</i>	<i>69 μsec</i>
0.0399	0.0374	0.0329	0.0325	0.0371	0.0439	0.0191	0.0433	0.0313	0.0255
0.0336	0.0479	0.0425	0.0307	0.0363	0.0424	0.0228	0.0364	0.0259	0.0301
0.0431	0.0421	0.0332	0.0247	0.0508	0.0331	0.0301	0.0287	0.0376	0.032
0.0355	0.0361	0.0355	0.0283	0.0448	0.0298	0.0229	0.0349	0.0392	0.0343
0.0381	0.0343	0.0391	0.0473	0.0444	0.0384	0.0383	0.0549	0.0339	0.0324
<b>0.03804</b>	<b>0.03956</b>	<b>0.03664</b>	<b>0.0327</b>	<b>0.04268</b>	<b>0.03752</b>	<b>0.02664</b>	<b>0.03964</b>	<b>0.03358</b>	<b>0.03086</b>
<i>70 μsec</i>	<i>71 μsec</i>	<i>72 μsec</i>	<i>73 μsec</i>	<i>74 μsec</i>	<i>75 μsec</i>	<i>76 μsec</i>	<i>77 μsec</i>	<i>78 μsec</i>	<i>79 μsec</i>
0.0409	0.0358	0.0378	0.0347	0.0226	0.0314	0.0277	0.0251	0.0278	0.0124
0.0363	0.0287	0.0329	0.0151	0.0152	0.0303	0.0145	0.0253	0.023	0.0253
0.0339	0.0289	0.0267	0.0341	0.0484	0.0124	0.0528	0.0295	0.0305	0.0287
0.0256	0.0355	0.0285	0.0375	0.0344	0.0304	0.0302	0.0309	0.0274	0.0271
0.0484	0.0358	0.0457	0.0335	0.0444	0.0405	0.024	0.032	0.0442	0.0372
<b>0.03702</b>	<b>0.03294</b>	<b>0.03432</b>	<b>0.03098</b>	<b>0.033</b>	<b>0.029</b>	<b>0.02984</b>	<b>0.02856</b>	<b>0.03058</b>	<b>0.02614</b>
<i>80 μsec</i>	<i>81 μsec</i>	<i>82 μsec</i>	<i>83 μsec</i>	<i>84 μsec</i>	<i>85 μsec</i>	<i>86 μsec</i>	<i>87 μsec</i>	<i>88 μsec</i>	<i>89 μsec</i>
0.022	0.0295	0.0301	0.0278	0.0216	0.0222	0.0266	0.0337	0.0342	0.0184
0.0117	0.0323	0.0265	0.0318	0.0229	0.0217	0.0263	0.0277	0.0303	0.0185
0.039	0.022	0.0227	0.034	0.0412	0.0283	0.0174	0.0209	0.0262	0.0226
0.0325	0.0148	0.0249	0.0283	0.0264	0.0408	0.0269	0.03	0.0197	0.0208
0.0357	0.0386	0.0288	0.0254	0.0365	0.0264	0.0363	0.0312	0.0355	0.037
<b>0.02818</b>	<b>0.02744</b>	<b>0.0266</b>	<b>0.02946</b>	<b>0.02972</b>	<b>0.02788</b>	<b>0.0267</b>	<b>0.0287</b>	<b>0.02918</b>	<b>0.02346</b>
<i>90 μsec</i>	<i>91 μsec</i>	<i>92 μsec</i>	<i>93 μsec</i>	<i>94 μsec</i>	<i>95 μsec</i>	<i>96 μsec</i>	<i>97 μsec</i>	<i>98 μsec</i>	<i>99 μsec</i>
0.0118	0.0055	0.0453	0.0197	0.0196	0.0122	0.021	0.0234	0.0173	0.0305
0.0169	0.0251	0.0294	0.0303	0.0224	0.0207	0.0212	0.0229	0.0134	0.0212
0.0172	0.0061	0.0168	0.0187	0.0184	0.0337	0.0182	0.0195	0.0181	0.0223
0.0499	0.0254	0.0265	0.0374	0.0254	0.0258	0.028	0.0285	0.0425	0.0108
0.0298	0.0354	0.0393	0.0327	0.0368	0.0311	0.0422	0.0232	0.0323	0.0201
<b>0.02845</b>	<b>0.023</b>	<b>0.028</b>	<b>0.029775</b>	<b>0.02575</b>	<b>0.027825</b>	<b>0.0274</b>	<b>0.023525</b>	<b>0.026575</b>	<b>0.0186</b>
<i>100 μsec</i>									
0.0069	0.0206	0.0206	0.0226	0.0308	<b>0.02365</b>				



## Appendix B – FFT-based Mixing efficiency

<i>10 μsec</i>	<i>11 μsec</i>	<i>12 μsec</i>	<i>13 μsec</i>	<i>14 μsec</i>	<i>15 μsec</i>	<i>16 μsec</i>	<i>17 μsec</i>	<i>18 μsec</i>	<i>19 μsec</i>
0.1383	0.106	0.1068	0.104	0.0932	0.0988	0.0936	0.1158	0.0837	0.1035
0.1062	0.1179	0.136	0.093	0.045	0.0402	0.044	0.0716	0.09	0.072
0.1447	0.124	0.078	0.071	0.0424	0.042	0.0396	0.0244	0.016	0.026
0.1756	0.1658	0.1149	0.0876	0.087	0.082	0.077	0.0664	0.0618	0.0776
0.1062	0.1395	0.1064	0.0924	0.0908	0.0772	0.0556	0.0596	0.0888	0.0808
<b>0.1342</b>	<b>0.13064</b>	<b>0.10842</b>	<b>0.0896</b>	<b>0.07168</b>	<b>0.06804</b>	<b>0.06196</b>	<b>0.06756</b>	<b>0.06806</b>	<b>0.07198</b>
<i>20 μsec</i>	<i>21 μsec</i>	<i>22 μsec</i>	<i>23 μsec</i>	<i>24 μsec</i>	<i>25 μsec</i>	<i>26 μsec</i>	<i>27 μsec</i>	<i>28 μsec</i>	<i>29 μsec</i>
0.0972	0.1242	0.0922	0.0535	0.0621	0.0702	0.0605	0.05265	0.0580	0.0999
0.0904	0.0963	0.0796	0.0787	0.0666	0.0661	0.0670	0.0621	0.0715	0.0706
0.054	0.0693	0.0882	0.0562	0.054	0.0846	0.1025	0.0625	0.063	0.1030
0.0711	0.0891	0.0895	0.0661	0.0607	0.0711	0.0715	0.0576	0.0666	0.0841
0.0324	0.0345	0.0455	0.0310	0.0895	0.0918	0.0846	0.0877	0.063	0.027
<b>0.06903</b>	<b>0.08271</b>	<b>0.07902</b>	<b>0.05715</b>	<b>0.0666</b>	<b>0.07677</b>	<b>0.07722</b>	<b>0.06453</b>	<b>0.06444</b>	<b>0.07695</b>
<i>30 μsec</i>	<i>31 μsec</i>	<i>32 μsec</i>	<i>33 μsec</i>	<i>34 μsec</i>	<i>35 μsec</i>	<i>36 μsec</i>	<i>37 μsec</i>	<i>38 μsec</i>	<i>39 μsec</i>
0.0885	0.1251	0.0835	0.0279	0.0445	0.1044	0.0855	0.0927	0.0747	0.0725
0.0918	0.0495	0.0522	0.0755	0.1053	0.0522	0.0639	0.0517	0.0832	0.0735
0.0715	0.0243	0.0072	0.0189	0.0589	0.0925	0.0936	0.0855	0.0679	0.0670
0.0958	0.0382	0.0373	0.0198	0.0234	0.0508	0.0198	0.0555	0.0355	0.0193
0.0576	0.094	0.0935	0.0994	0.0364	0.0441	0.0576	0.0963	0.1015	0.0486
<b>0.08025</b>	<b>0.06633</b>	<b>0.05463</b>	<b>0.04824</b>	<b>0.05373</b>	<b>0.06876</b>	<b>0.06408</b>	<b>0.07632</b>	<b>0.07254</b>	<b>0.05616</b>
<i>40 μsec</i>	<i>41 μsec</i>	<i>42 μsec</i>	<i>43 μsec</i>	<i>44 μsec</i>	<i>45 μsec</i>	<i>46 μsec</i>	<i>47 μsec</i>	<i>48 μsec</i>	<i>49 μsec</i>
0.0187	0.0665	0.0515	0.1107	0.0702	0.1134	0.0675	0.0333	0.1075	0.0705
0.0202	0.0486	0.0855	0.1314	0.0345	0.0423	0.0657	0.0595	0.0375	0.0441
0.0395	0.1105	0.126	0.1089	0.1377	0.0351	0.0105	0.0765	0.09	0.0666
0.1005	0.1062	0.0702	0.0335	0.0485	0.0765	0.0955	0.0531	0.0585	0.0345
0.0513	0.0475	0.0655	0.0285	0.054	0.0477	0.0385	0.0725	0.0625	0.0819
<b>0.04595</b>	<b>0.07605</b>	<b>0.07965</b>	<b>0.08262</b>	<b>0.06768</b>	<b>0.063</b>	<b>0.05607</b>	<b>0.0594</b>	<b>0.07056</b>	<b>0.06066</b>
<i>50 μsec</i>	<i>51 μsec</i>	<i>52 μsec</i>	<i>53 μsec</i>	<i>54 μsec</i>	<i>55 μsec</i>	<i>56 μsec</i>	<i>57 μsec</i>	<i>58 μsec</i>	<i>59 μsec</i>
0.074	0.08	0.0196	0.0196	0.0364	0.0464	0.0744	0.02	0.046	0.0844
0.0776	0.0928	0.0276	0.0276	0.0148	0.0716	0.0384	0.0136	0.0684	0.0908
0.0532	0.0492	0.0504	0.0504	0.034	0.0792	0.0196	0.044	0.0708	0.0624

0.0684	0.0544	0.0348	0.0348	0.0492	0.0088	0.0428	0.0428	0.0408	0.0464
0.0504	0.0644	0.0972	0.0972	0.0384	0.0848	0.0696	0.0516	0.0412	0.0728
<b>0.06472</b>	<b>0.06816</b>	<b>0.04592</b>	<b>0.04592</b>	<b>0.03456</b>	<b>0.05816</b>	<b>0.04896</b>	<b>0.0344</b>	<b>0.05344</b>	<b>0.07136</b>
<i>60 μsec</i>	<i>61 μsec</i>	<i>62 μsec</i>	<i>63 μsec</i>	<i>64 μsec</i>	<i>65 μsec</i>	<i>66 μsec</i>	<i>67 μsec</i>	<i>68 μsec</i>	<i>69 μsec</i>
0.0785	0.0525	0.098	0.0365	0.0441	0.0476	0.0567	0.0155	0.0399	0.0385
0.0615	0.0651	0.0595	0.0715	0.0505	0.0505	0.0555	0.035	0.0511	0.0189
0.0185	0.0056	0.0735	0.0294	0.0644	0.0553	0.0658	0.0505	0.028	0.0665
0.0437	0.0444	0.0574	0.0505	0.0658	0.0322	0.0469	0.0259	0.0845	0.0065
0.0147	0.0445	0.0238	0.0511	0.0371	0.0525	0.0441	0.0749	0.0651	0.0505
<b>0.04354</b>	<b>0.04242</b>	<b>0.06244</b>	<b>0.04907</b>	<b>0.05243</b>	<b>0.049</b>	<b>0.05383</b>	<b>0.04018</b>	<b>0.05369</b>	<b>0.03619</b>
<i>70 μsec</i>	<i>71 μsec</i>	<i>72 μsec</i>	<i>73 μsec</i>	<i>74 μsec</i>	<i>75 μsec</i>	<i>76 μsec</i>	<i>77 μsec</i>	<i>78 μsec</i>	<i>79 μsec</i>
0.0567	0.0387	0.0096	0.0474	0.0525	0.0663	0.0363	0.0801	0.0183	0.021
0.0531	0.0726	0.0663	0.0582	0.0336	0.0393	0.0261	0.0684	0.0471	0.0171
0.0048	0.0096	0.0159	0.0585	0.0231	0.0351	0.0555	0.0303	0.0477	0.0525
0.0183	0.0591	0.0618	0.0168	0.0618	0.0375	0.0726	0.0651	0.048	0.0216
0.0606	0.054	0.0417	0.0714	0.0504	0.0528	0.0552	0.0522	0.0312	0.0897
<b>0.0387</b>	<b>0.0468</b>	<b>0.03906</b>	<b>0.05046</b>	<b>0.04428</b>	<b>0.0462</b>	<b>0.04914</b>	<b>0.05922</b>	<b>0.03846</b>	<b>0.04038</b>
<i>80 μsec</i>	<i>81 μsec</i>	<i>82 μsec</i>	<i>83 μsec</i>	<i>84 μsec</i>	<i>85 μsec</i>	<i>86 μsec</i>	<i>87 μsec</i>	<i>88 μsec</i>	<i>89 μsec</i>
0.0723	0.0396	0.0282	0.0354	0.0447	0.0513	0.0612	0.0519	0.0231	0.0555
0.0849	0.0525	0.0165	0.0426	0.0285	0.063	0.0264	0.0186	0.0366	0.0201
0.0225	0.0168	0.0477	0.057	0.0426	0.0615	0.0468	0.0429	0.0144	0.0396
0.0318	0.0741	0.0537	0.0567	0.0414	0.0564	0.0459	0.0522	0.0564	0.0345
0.0342	0.0258	0.0537	0.0339	0.0483	0.072	0.0519	0.021	0.0612	0.0219
<b>0.04914</b>	<b>0.04176</b>	<b>0.03996</b>	<b>0.04512</b>	<b>0.0411</b>	<b>0.06084</b>	<b>0.04644</b>	<b>0.03732</b>	<b>0.03834</b>	<b>0.03432</b>
<i>90 μsec</i>	<i>91 μsec</i>	<i>92 μsec</i>	<i>93 μsec</i>	<i>94 μsec</i>	<i>95 μsec</i>	<i>96 μsec</i>	<i>97 μsec</i>	<i>98 μsec</i>	<i>99 μsec</i>
0.0506	0.0206	0.032	0.0332	0.0304	0.052	0.0436	0.0258	0.0226	0.0242
0.035	0.0342	0.0262	0.0592	0.0394	0.0338	0.0362	0.0266	0.0414	0.0388
0.0372	0.0423	0.0213	0.0738	0.0399	0.0567	0.0591	0.0483	0.0438	0.0129
0.0396	0.0309	0.0207	0.0411	0.0264	0.0138	0.0375	0.0411	0.0402	0.0297
0.0555	0.051	0.0363	0.0693	0.0393	0.0423	0.0177	0.0318	0.0366	0.0225
<b>0.04358</b>	<b>0.0358</b>	<b>0.0273</b>	<b>0.05532</b>	<b>0.03508</b>	<b>0.03972</b>	<b>0.03882</b>	<b>0.03472</b>	<b>0.03692</b>	<b>0.02562</b>
<i>100 μsec</i>									
0.0213	0.0216	0.0336	0.045	0.06	<b>0.0363</b>				

## Bibliography

- [1] Andrews, L. and R. Phillips. *Laser Beam Propagation through Random Media*. SPIE, Bellingham, WA, second edition, 2005.
- [2] Cain, S. C. *Improved Atmospheric Turbulence Tilt-Estimation and its Effect on Astronomical Imaging*. Thesis, University of Dayton. Dayton OH, 2001.
- [3] Cain S. C., and R. D. Richmond. *Direct-Detection LADAR Systems*. SPIE. Bellingham WA, 2010.
- [4] Deas, B. T. *Pulse shape Correlation for Laser detection and Ranging (LADAR)*. Thesis, Air Force Institute of Technology. WPAFB OH, 2010.
- [5] Gebhart, B., Jaluria, Y., Mahajan, R.L., and B. Sammakia. *Buoyancy-Induced Flows and Transport*, Hemisphere, Cambridge (1988).
- [6] Goodman, J. W. *Introduction to Fourier Optics*. Roberts & Company Publishers, Greenwood Village CO, 2005.
- [7] Goodman, J. W. *Statistical Optics*. John Wiley and Sons, Inc., New York NY, 1985
- [8] E. P. Goodwin, and J. C. Wyant. *Field Guide to Interferometric Optical Testing*. The International Society for Optical Engineering. Bellingham, WA: 2006
- [9] R. G. Lane, A. D. Glindemann A, and J. C. Dainty. "Simulation of a Kolmogorov phase screen." *Waves in Random Media*, Vol 2, Issue 3, pg 209-224, Imperial College, London. 1992
- [10] Noll, Robert J. "Zernike Polynomials and Atmospheric Turbulence." *Optical Society of America* 66. Mar (1976): 207-11.
- [11] I. B. Putnam and S. C. Cain. "Modeling a Temporally Evolving Atmosphere with Zernike Polynomials." AMOS Proceedings. Kihei HI, 2012.
- [12] C. J. Pellizzari, C. L. Matson, and R. Gudimetla. "Inverse synthetic aperture LADAR for geosynchronous space objects – signal-to-noise analysis." AMOS Proceedings. Kihei HI, 2011.
- [13] N. D. Roddier. "Atmospheric wavefront simulation using Zernike polynomials." *Optical Engineering* 29(10), Oct. (1990): 1174-1180.

- [14] Schmidt, J. *Numerical Simulation of Optical wave Propagation, With Examples in MATLAB*. SPIE. Bellingham WA, 2010.
- [15] Welsh, B. M. "Fourier-series-based Atmospheric Phase Screen Generator for Simulating Anisoplanatic Geometries and temporal Evolution," *Proc. SPIE* 3125, Propagation and Imaging through the Atmosphere, 327 (Sept 23, 1997).

# REPORT DOCUMENTATION PAGE

*Form Approved*  
OMB No. 074-0188

The public reporting burden for this collection of information is estimated to average 1 hour per response, including the time for reviewing instructions, searching existing data sources, gathering and maintaining the data needed, and completing and reviewing the collection of information. Send comments regarding this burden estimate or any other aspect of the collection of information, including suggestions for reducing this burden to Department of Defense, Washington Headquarters Services, Directorate for Information Operations and Reports (0704-0188), 1215 Jefferson Davis Highway, Suite 1204, Arlington, VA 22202-4302. Respondents should be aware that notwithstanding any other provision of law, no person shall be subject to any penalty for failing to comply with a collection of information if it does not display a currently valid OMB control number.

**PLEASE DO NOT RETURN YOUR FORM TO THE ABOVE ADDRESS.**

<b>1. REPORT DATE</b> (DD-MM-YYYY) 21 March 2013		<b>2. REPORT TYPE</b> Master's Thesis		<b>3. DATES COVERED</b> (From - To) 1 Sept 2011 - 21 March 2013	
<b>4. TITLE AND SUBTITLE</b> Atmospheric Impact on Long Pulse Laser Detection and Ranging (LADAR) Systems				<b>5a. CONTRACT NUMBER</b>	
				<b>5b. GRANT NUMBER</b>	
				<b>5c. PROGRAM ELEMENT NUMBER</b>	
<b>6. AUTHOR(S)</b> Putnam, Isaac B., 1st Lt., USAF				<b>5d. PROJECT NUMBER</b> N/A	
				<b>5e. TASK NUMBER</b>	
				<b>5f. WORK UNIT NUMBER</b>	
<b>7. PERFORMING ORGANIZATION NAMES(S) AND ADDRESS(S)</b> Air Force Institute of Technology Graduate School of Engineering and Management (AFIT/EN) 2950 Hobson Way, Building 640 WPAFB OH 45433				<b>8. PERFORMING ORGANIZATION REPORT NUMBER</b>  AFIT-ENG-13-M-39	
<b>9. SPONSORING/MONITORING AGENCY NAME(S) AND ADDRESS(ES)</b>  Intentionally Left Blank				<b>10. SPONSOR/MONITOR'S ACRONYM(S)</b> N/A	
				<b>11. SPONSOR/MONITOR'S REPORT NUMBER(S)</b>	
<b>12. DISTRIBUTION/AVAILABILITY STATEMENT</b> APPROVED FOR PUBLIC RELEASE; DISTRIBUTION UNLIMITED					
<b>13. SUPPLEMENTARY NOTES</b>					
<b>14. ABSTRACT</b> For conventional imaging systems, GEO space objects cannot be resolved due to their 40 Mm distance. There exists a strong need to obtain high resolution images of GEO objects and to accomplish this task, investigation into the suitability of ISAL is currently underway. A critical component in determining this suitability is to accurately model the atmospheric impacts on LADAR pulses. Conventional knowledge says that while the atmosphere churns, wind is the predominant cause of temporal evolution which simplifies all modeling and simulation into the frozen flow hypothesis. The concern is that the frozen flow hypothesis based phase screen generation techniques fail to accurately predict the temporal development of optical phase. This thesis proposes a new approach and provides a detailed derivation of a new temporally evolving Zernike polynomial based atmospheric phase screen generation model. This new model is experimentally verified, and utilized to analyze atmospheric impacts on mixing efficiencies. It is shown that this new turbulent flow model more accurately predicts mixing efficiency than that of the basic frozen flow approximation.					
<b>15. SUBJECT TERMS</b> Turbulent-flow phase screen generation, ISAL, Zernike polynomial temporal correlation					
<b>16. SECURITY CLASSIFICATION OF:</b>			<b>17. LIMITATION OF ABSTRACT</b>	<b>18. NUMBER OF PAGES</b>	<b>19a. NAME OF RESPONSIBLE PERSON</b>
<b>a. REPORT</b>	<b>b. ABSTRACT</b>	<b>c. THIS PAGE</b>			<b>19b. TELEPHONE NUMBER</b> (Include area code)
U	U	U	UU	69	Cain, Stephen C., PhD (937) 255-6565, x 4716 (stephen.cain@afit.edu)